

**Investigating the Effects of Upper Lapse Rate and
Surface Heat Flux on an idealized Convective
Atmospheric Boundary Layer Entrainment Layer
using Large Eddy Simulation**

by

Niamh Chaparro

A THESIS SUBMITTED IN PARTIAL FULFILLMENT
OF THE REQUIREMENTS FOR THE DEGREE OF

MSc

in

THE FACULTY OF GRADUATE STUDIES
(Earth, Ocean and Atmospheric Sciences)

The University Of British Columbia
(Vancouver)

missing submission month missing submission year

© Niamh Chaparro, *missing submission year*

Table of Contents

Table of Contents	ii
List of Figures	iv
Glossary	vi
1 Introduction	1
1.1 Motivation	1
1.2 Relevant Background	2
1.2.1 The Convective Boundary Layer (CBL)	2
1.2.2 CBL Height (h)	5
1.2.3 CBL Growth by Entrainment	7
1.2.4 The CBL Entrainment Layer (EL)	7
1.2.5 Modelling the CBL and EL	9
1.2.6 Scales and Scaling Relations of the CBL and EL	13
1.3 Research Questions	18
1.4 Approach to Research Questions	20
2 Research Questions Answered using Model Output	24
2.1 Verifying the Model Output	26
2.1.1 Initialization and Spin-Up Time	26
2.1.2 Horizontally and Ensemble averaged vertical Potential Temperature $\bar{\theta}$ and Heat Flux $\overline{w'\theta'}$ Profiles	29
2.1.3 FFT Energy Spectra	31
2.1.4 Visualization of Structures Within the Entrainment Layer	33

2.1.5	Summary of Findings	33
2.2	Local Statistics (Q1)	35
2.2.1	Local Mixed Layer Heights (h_0^l)	35
2.2.2	Local turbulent Velocity and Potential Temperature Fluctuations	39
2.2.3	Downward Moving Warm Air at h	42
2.2.4	Answer to Q1	44
2.3	Relationship of Entrainment Layer Depth to Richardson Num- ber (Q2)	46
2.3.1	Threshold Test for lower EL Limit, h_0	49
2.3.2	EL Limits based on scaled vertical Profiles	51
2.3.3	Answer to Q2	53
2.4	Relationship of Entrainment Rate to Richardson Number (Q3)	54
2.4.1	Reminder of Definitions	54
2.4.2	CBL Growth	54
2.4.3	Heights based on the scaled vertical average Potential Temperature Profile	58
2.4.4	Heights based on the scaled vertical average Heat Flux Profile	60
2.4.5	Answer to Q3	62
References	63
A Appendices	66
A.1	Potential Temperature: θ	66
A.2	Second Law of Thermodynamics	67
A.3	Reynolds Decomposition and Simplification of Conservation of Enthalpy (or Entropy) for a dry Atmosphere	67
A.4	Reynolds averaged Turbulence Kinetic Energy Equation	68

List of Figures

Figure 1.1	Lidar backscatter image of the CBL	3
Figure 1.2	Visualization of entrainment from an LES	4
Figure 1.3	Idealized vertical average profiles for a dry CBL	5
Figure 1.4	Zero order CBL	10
Figure 1.5	Height definitions	23
Figure 2.1	Scaled time vs Time	27
Figure 2.2	Vertical profiles of $\bar{\theta}$, $\frac{\partial \bar{\theta}}{\partial z}$ and $\overline{w' \theta'}$	28
Figure 2.3	$\overline{w' \theta'}$ scaled by $(\overline{w' \theta'})_s$	28
Figure 2.4	$\bar{\theta}$ profiles at 2 hours for all runs	29
Figure 2.5	Scaled $(\overline{w' \theta'})_s$ profiles at 2 hours for all runs	30
Figure 2.6	FFT energy spectra of w'	32
Figure 2.7	2D horizontal slices of θ' and w'	34
Figure 2.8	High local ML	36
Figure 2.9	Low local ML	36
Figure 2.10	Local ML height distributions	37
Figure 2.11	Scaled local ML height PDFs	38
Figure 2.12	2D distributions of w' and θ' for all runs	40
Figure 2.13	Scaled 2D distributions of w' and θ' for all runs	41
Figure 2.14	Downward moving warm air at h	42
Figure 2.15	Downward turbulent velocity perturbation at h	43
Figure 2.16	Positive potential temperature perturbation at h (i)	43
Figure 2.17	Positive potential temperature perturbation at h (ii)	44
Figure 2.18	Scaled EL limits	46
Figure 2.19	Vertical $\frac{\partial \bar{\theta}}{\partial z}$ profiles with threshold at .0002	47

Figure 2.20 Scaled EL depth ($\frac{h_1}{h} - \frac{h_0}{h}$) vs inverse Richardson Number with threshold at .0002	48
Figure 2.21 Scaled EL depth vs inverse Richardson Number with threshold at .0004	49
Figure 2.22 Scaled EL depth vs inverse bulk Richardson Number with threshold at .0001	50
Figure 2.23 Scaled vertical $\frac{\partial \bar{\theta}}{\partial z}$ profiles with threshold at .03	51
Figure 2.24 scaled EL depth vs Ri^{-1}	52
Figure 2.25 Log-log plot of scaled EL depth vs Ri^{-1}	52
Figure 2.26 Height definitions	54
Figure 2.27 h vs time for all runs	56
Figure 2.28 h vs time for all runs on log-log coordinates	56
Figure 2.29 $\frac{z_f}{h}$ vs Time	57
Figure 2.30 Richardson numbers based on $\frac{\frac{\partial \bar{\theta}}{\partial z}}{\gamma}$	58
Figure 2.31 Scaled entrainment rate vs inverse Richardson number (i)	59
Figure 2.32 Richardson numbers based on $\frac{\overline{w' \theta'}}{\overline{w' \theta'}_s}$	60
Figure 2.33 Scaled entrainment rate vs inverse Richardson number (ii)	61

Glossary

CBL Convective Boundary Layer

DNS Direct Numerical Simulation

EL Entrainment Layer

FA Free Atmosphere

FFT Fast Fourier Transform

GCM General Circulation Model

ML Mixed Layer

LES Large Eddy Simulation

Ri Richardson Number, the bulk Richardson Number is $\frac{gh}{\bar{\theta}_{ML} w^{*2}} \frac{\Delta\theta}{\bar{\theta}(h_1) - \bar{\theta}(h_0)}$, $\Delta\theta =$

TKE Turbulence Kinetic Energy

1. Introduction

1.1 Motivation

The daytime convective atmospheric boundary layer (CBL) over land starts to grow at sunrise when the surface becomes warmer than the air above it. Coherent turbulent structures (thermals) begin to form and rise since their relative warmth causes them to be less dense than their surroundings and so buoyant. The temperature profile of the residual nighttime boundary layer is stable i.e. potential temperature (θ , see Section A.1) increases with height. The thermals rise to their neutral buoyancy level overshoot and then overturn or recoil concurrently trapping or enveloping warm stable air from the free atmosphere (FA) above them which is subsequently mixed into the growing turbulent mixed layer (ML) (Stull 1988). This mixing at the top of the CBL is known as entrainment and the region over which it occurs, the entrainment layer (EL). A common, simplified conceptual model of this case is the dry shear free CBL (Sullivan et al. 1998, Federovich et al. 2004 Brooks and Fowler 2012). This model serves as an intellectually accessible way to understand the dynamic and complex CBL and its EL.

CBL height (h) and the prediction thereof are important for calculating the concentration of any atmospheric species as well as the sizes of the turbulent structures. In combination with the level at which clouds condense (lifting condensation level) knowledge of EL depth facilitates predictions pertaining to the formation of cumulus clouds. For example cloud cover increases as more thermals rise above their lifting condensation level. Parameterizations

for both CBL growth and EL depth are required in mesoscale and general circulation models (GCMs). Furthermore it is an attractive goal to develop a robust set of scales for this region analogous to Monin-Obukov Theory (Stull 1988, Traumner et al. 2011, Steyn et al. 1999, Nelson et al. 1989, Sorbjan 1996).

Atmospheric CBL entrainment has been studied as a separate phenomenon (Nelson et al. 1989, Sullivan et al. 1998, Federovich et al. 2004, Brooks and Fowler 2012) as well as within the wider topic of entrainment in geophysical flows (Turner 1986). There is broad agreement as to the fundamental scaling parameters and relationships involved. However, the discussion as to how the parameters are defined and measured (Brooks and Fowler 2012, Traumner et al. 2011) and the exact forms of the resulting relationships continues (Sullivan et al. 1998, Federovich et al. 2004 Brooks and Fowler 2012). This prompts me to ask the research questions I build up to in Section 1.2 and outline in Section 1.3.

1.2 Relevant Background

1.2.1 The Convective Boundary Layer (CBL)

The CBL starts to grow rapidly at sunrise, peaking at midday. Convective turbulence and the dominant upward vertical motions then begin to subside as the surface cools. While the surface is warm, buoyancy driven thermals of uniform potential temperature (θ) and tracer concentration at their cores form and entrain surrounding air laterally as they rise, as well as trapping and mixing in stable warm from above (Stull 1988, Crum et al. 1987). Under conditions of strong convection, buoyantly driven turbulence dominates and shear is insignificant (Fedorovich and Conzemius 2001). Thermal overshoot relative to their neutral buoyancy level, and subsequent entrainment of the warmer air from aloft augments the warming caused by the surface turbulent heat flux ($\overline{w'\theta'}$)_s (see Section A.1) and results in a θ jump or inversion at the CBL top (Schmidt and Schumann 1989, Turner 1986). There may

also be a residual inversion from the day before, possibly strengthened by subsidence (Stull 1988, Sullivan et al. 1998).

Lidar images such as Figure 1.1 show the overall structure of the CBL with rising thermals, impinging on the air above (Crum et al. 1987, Traumner et al. 2011).

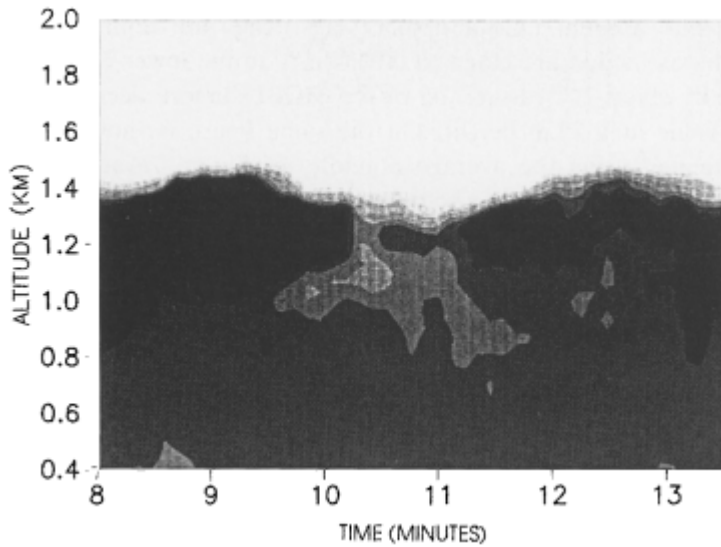


Figure 1.1: Lidar backscatter image of the CBL from DuPont et al. 1994. The horizontal distance between the two peaks corresponds to approximately 1700 meters.

This has been effectively modelled using large eddy simulation (LES) by Schmidt and Schumann (1989) who used horizontal slices of turbulent potential temperature and vertical velocity fluctuations (θ' , w') at various vertical levels to show how the thermals form, merge and impinge at the CBL top with concurrent peripheral downward motions. The latter is supported in the LES visualizations of Sullivan et al. (1998). The vertical cross section within the EL in Figure 1.2 shows the relatively cooler thermals and trapped warmer air as well as the closely associated upward motion of cooler air and downward motion of warmer air.

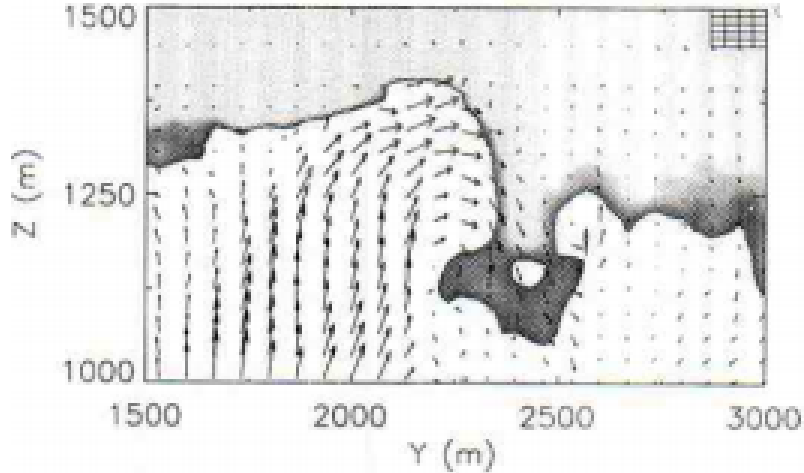


Figure 1.2: Flow visualization from Sullivan et al. 1998 showing a modelled CBL thermal enveloping FA air.

On average these convective turbulent structures create a fully turbulent mixed layer (ML) with eddy sizes cascading through an inertial subrange to the molecular scales at which energy is lost via viscous dissipation (Stull 1988). Here, as represented in Figure 1.3, $\bar{\theta}$ is close to uniform and increases with respect to time due to $(\overline{w'\theta'})_s$ and the downward flux of entrained stable air at the inversion $(\overline{w'\theta'})_h$. ML turbulence is dominated by warm updraughts and cool downdraughts. With proximity to the top the updraughts become relatively cool and warmer FA air from above is drawn downward, so in the ML $\overline{w'\theta'}$ is positive and decreasing. Directly above the ML the air is stable with intermittent turbulence and, on average, transitions from a uniform ML potential temperature ($\frac{\partial \bar{\theta}}{\partial z} \approx 0$) to a stable lapse rate (γ). A peak in the average vertical gradient ($\frac{\partial \theta}{\partial z}$) at the inversion represents regions where thermals have exceeded their neutral buoyancy level (see Figure 1.3).

Nelson et al. (1989) outline the stages of CBL growth from when the sub-layers of the nocturnal boundary layer are entrained, until the previous day's capping inversion is reached and a quasi-steady growth is attained. The EL depth relative to CBL height varies throughout these stages and its

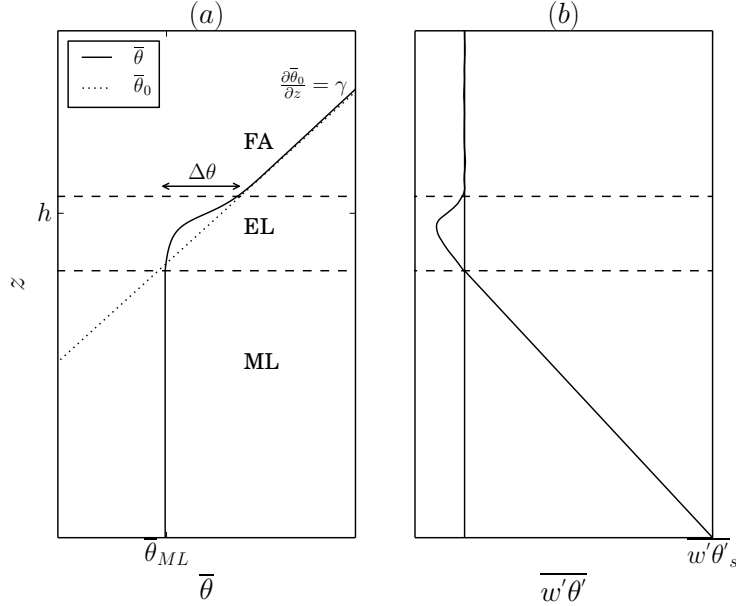


Figure 1.3: Idealized vertical average profiles for a dry CBL in the absence of large scale winds or subsidence. (a) $\bar{\theta}_{ML}$ is the average mixed layer potential temperature. h is the height of maximum gradient in the $\bar{\theta}$ profile. $\bar{\theta}_0$ (dotted line) is the initial $\bar{\theta}$ profile which has a slope γ . The mixed layer, entrainment layer and free atmosphere are denoted ML, EL and FA respectively. (b) $w'\theta'$ is the average surface turbulent heat flux. The EL limits (dashed lines) enclose the region of negative $w'\theta'$.

relationship to scaled entrainment is hysteretic. Numerical studies typically represent this last quasi-steady phase involving a constant $(w'\theta')_s$ working against an inversion and or a stable γ (Schmidt and Schumann 1989, Sorbjan 1996, Sullivan et al. 1998, Federovich et al. 2004, Brooks and Fowler 2012, Garcia and Mellado 2014).

1.2.2 CBL Height (h)

The ML is fully turbulent with a uniform average potential temperature ($\bar{\theta}$) which increases sharply over the EL . Aerosol and water vapour concentra-

tions decrease dramatically with transition to the stable upper FA. So any of these characteristics can support a definition of CBL height (h). Nelson et al. (1989) defined h in terms of the percentage of ML air and identified it by eye from Lidar back-scatter images. Traumner et al. (2011) compared four automated methods applied to Lidar images:

- a suitable threshold value above which the air is categorized as ML air,
- the point of minimum (largest negative) vertical gradient,
- the point of minimum vertical gradient based on a fitted idealized curve,
- and the maximum wavelet covariance.

CBL height detection is a wide and varied field. Both Brooks and Fowler (2012) and Traumner et al. 2011 provide more thorough reviews.

Numerical models produce hundreds of local horizontal points from which smooth averaged vertical profiles are obtained, and statistically robust relationships inferred. Brooks and Fowler (2012) applied a wavelet technique to identify the height of maximum covariance in local vertical tracer profiles in their LES study. They compared this method to the gradient method i.e. locating the height of most negative vertical gradient, as well as the height of minimum $\overline{w'\theta'}$ as shown later in Figure 1.5. This last definition is common among LES and laboratory studies where it has been referred to as the inversion height (Deardorff et al. 1980, Sorbjan 1999, Federovich et al. 2004). Sullivan et al. (1998) clarified that the extrema of the four $\overline{w'\theta'}$ quadrants (upward warm: $\overline{w'+\theta'^+}$, downward warm: $\overline{w'-\theta'^+}$, upward cool: $\overline{w'+\theta'^-}$, downward cool: $\overline{w'-\theta'^-}$) in the EL more or less correspond to the average point of maximum $\frac{\partial \theta}{\partial z}$ (see h in Figure 1.3), whereas the point of minimum $\overline{w'\theta'}$ was consistently lower. They defined CBL height based on local $\frac{\partial \theta}{\partial z}$ and applied horizontal averaging as well as two methods based on $\overline{w'\theta'}$ for comparison.

1.2.3 CBL Growth by Entrainment

The CBL grows by trapping pockets of warm stable air between or adjacent to impinging thermal plumes. Traumner et al. (2011) summarize two categories of CBL entrainment:

- Non turbulent fluid can be engulfed between or in the overturning of thermal plumes. This kind of event has been supported by the visualizations in Sullivan et al.'s (1998) LES study as well as in Traumner et al.'s (2011) observations. In both it appeared to occur under a weak inversion or upper lapse rate (γ)
- Impinging thermal plumes distort the inversion interface dragging wisps of warm stable air down at their edges or during recoil under a strong inversion or lapse rate. This type of event is supported by the findings of both Sullivan et al. (1998) and Traumner et al. (2011).

Shear induced instabilities do occur at the top of the atmospheric boundary layer and in some laboratory studies of turbulent boundary layers, under conditions of very high stability, breaking of internal waves have been observed. Entrainment via the former is relatively insignificant in strong convection, and the latter has not been directly observed in real or modeled atmospheric CBLs over the range of conditions considered here (Traumner et al. 2011, Sullivan et al. 1998).

1.2.4 The CBL Entrainment Layer (EL)

The ML is fully turbulent but the top is characterized by stable air with intermittent turbulence due to the higher reaching thermals. Garcia and Mellado (2014) demonstrate that the EL is subdivided in terms of length and buoyancy scales. That is, the lower region is comprised of mostly turbulent air with pockets of stable warmer air that are quickly mixed, and so scales with the convective scales (see section 1.2.6). Whereas the upper region is mostly stable apart from the impinging thermals so scaling here is more influenced by the lapse rate (γ). In the EL the average vertical heat

flux, $\overline{w'\theta'}$, switches sign relative to that in the ML. The fast updraughts are now relatively cool $\overline{w'+\theta'-}$. In their analysis of the four $\overline{w'\theta'}$ quadrants Sullivan et al. (1998) concluded that the net dynamic in this region is downward motion of warm air ($\overline{w'-\theta'+}$) from the free atmosphere (FA) since the other three quadrants effectively cancel.

In terms of tracer concentration, and for example based on a Lidar backscatter profile, there are two ways to conceptually define the EL. It can be thought of as the range in space (or time) over which local CBL height varies (Crum et al. 1987) or a local region over which the concentration (or back-scatter intensity) transitions from ML to FA values (Traumner et al. 2011). The latter can be estimated using either curve-fitting or wavelet techniques (Traumner et al. 2011, Steyn et al. 1999, Brooks and Fowler 2012).

Brooks and Fowler apply a wavelet technique to tracer profiles for the determination of EL limits, in their 2012 LES study. However, it is more common in numerical modelling and laboratory studies for the EL limits to be defined based on the average vertical turbulent heat flux ($\overline{w'\theta'}$) i.e. the points enclosing the negative region as shown in Figure 1.3 (Deardorff et al. 1980, Federovich et al. 2004, Garcia and Mellado 2014). Bulk models based on the representation in Figure 1.3 assume the region of negative $\overline{w'\theta'}$ coincides with the region where $\bar{\theta}$ transitions from the ML value to the FA value (Deardorff 1979, Federovich et al. 2004) but no modelling studies use the vertical $\bar{\theta}$ profile to define the EL.

Since $\bar{\theta}$ modeled by an LES is not strictly constant with respect to height in the ML (Federovich et al. 2004), a threshold value for $\bar{\theta}$ or its vertical gradient must be chosen to identify the lower EL limit. In their 2012 LES study Brooks and Fowler encountered inconsistencies when determining the EL limits from the average tracer profile. Although their tracer profile was quite different to a simulated CBL $\bar{\theta}$ profile, this could serve as cautionary note.

Our understanding of the characteristics and dynamics of the atmospheric CBL entrainment layer evolves with the increasing body of measurement (Traumner et al. 2011, Nelson et al. 1989), laboratory (Deardorff et al. 1980) and numerical studies (Deardorff 1972, Sorbjan 1996, Sullivan et al. 1998, Federovich et al. 2004, Brooks and Fowler 2012, Garcia and Mellado 2014). Parameterizations for CBL growth and EL depth are derived based on bulk models and are evaluated using LES output and measurements (Federovich et al. 2004, Boers 1989). So the relationship between theory, numerical simulation and measurement is inextricable and any study based on one must refer to at least one of the others.

1.2.5 Modelling the CBL and EL

Bulk Models

Bulk models for the Convective Boundary layer (CBL) based on average, vertical profiles of ML quantities can be subdivided into: (i) zero order as represented in Figure 1.4 and (ii) first (and higher) order bulk models as represented in Figure 1.3. Order refers to the number of prognostic variables, and increased order corresponds to increasing complexity in the shape of the $\bar{\theta}$ and $\overline{w'\theta'}$ profiles at the top of the ML.

Zero order bulk models assume an ML of uniform potential temperature ($\bar{\theta}_{ML}$) topped by an infinitesimally thin layer across which there is a temperature jump ($\delta\theta$) and above which is a constant lapse rate (γ). The assumed average vertical turbulent heat flux, $\overline{w'\theta'}$, decreases linearly from the surface up, reaching a maximum negative value $(\overline{w'\theta'})_h$. This is a constant proportion of the surface value, usually $-2(\overline{w'\theta'})_s$ (see Section 4 in Tennekes 1973 for a discussion). At the temperature inversion $\overline{w'\theta'}$ jumps to zero across the infinitesimally thin layer. Equations for the evolution of CBL height, $\bar{\theta}_{ML}$ and $\delta\theta$ are derived on this basis (Tennekes 1973).

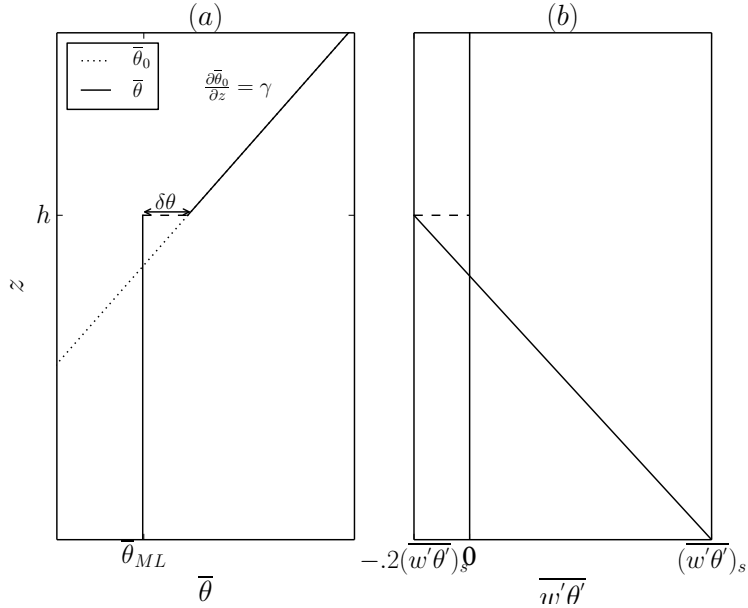


Figure 1.4: Simplified version of Figure 1.3 such that the EL is infinitesimally thin. (a) h is the height of the inversion and $\delta\theta$ the corresponding temperature jump, that is, the difference between $\bar{\theta}_{ML}$ and $\bar{\theta}_0(h)$. This is different, although related, to the jump across the EL in Figure 1.3 $\Delta\theta$. (b) The $w'\theta'$ profile is linear and decreasing until it reaches a maximum negative value at h of $-.2(\overline{w'\theta'})_s$. Here there is a discontinuity as it jumps to zero.

If the CBL height (h) is rising, air is being drawn in from the stable free atmosphere (FA) layer above and cooled i.e. it is decreasing in enthalpy. The rate of decrease in enthalpy with respect to time is $c_p\rho\delta\theta\frac{dh}{dt}$ (see Section A.1) per unit of horizontal area where $\frac{dh}{dt}$ is the entrainment rate (w_e). Since the lapse rate above the inversion is stable Tennekes (1973) equates this enthalpy loss to the average vertical turbulent heat flux at the inversion

$$\delta\theta\frac{dh}{dt} = -(\overline{w'\theta'})_h. \quad (1.1)$$

The ML warming rate is arrived at via the simplified Reynolds averaged

conservation of enthalpy, for which the full derivation is shown in Section A.3.

$$\frac{\partial \bar{\theta}_{ML}}{\partial t} = -\frac{\partial}{\partial z} \overline{w' \theta'}. \quad (1.2)$$

Assuming $\overline{w' \theta'}$ has a constant slope this becomes

$$\frac{\partial \bar{\theta}_{ML}}{\partial t} = \frac{(\overline{w' \theta'})_s - (\overline{w' \theta'})_h}{h} \quad (1.3)$$

and the evolution of the temperature jump ($\delta\theta$) depends on the rate of CBL height (h) increase, the upper lapse rate γ and the ML warming rate

$$\frac{d\delta\theta}{dt} = \gamma \frac{dh}{dt} - \frac{d\bar{\theta}_{ML}}{dt}. \quad (1.4)$$

An assumption about the vertical heat flux at the inversion (h), such as the entrainment ratio, closes this set

$$\frac{(\overline{w' \theta'})_h}{(\overline{w' \theta'})_s} = -.2. \quad (1.5)$$

The relevant quantities in equations 2.2 through 2.5 are idealized, ensemble averages. There is some variation within this class of model. For example the rate equation for h (entrainment relation) can alternatively be derived based on the turbulent kinetic energy budget (Federovich et al. 2004) but they are all based on the simplified $\bar{\theta}$ and $\overline{w' \theta'}$ profiles outlined above.

First (and higher) order models assume an EL of finite depth at the top of the ML, defined by two heights: the top of the ML (h_0) and the point where FA characteristics are resumed (h_1). The derivations are more complex and involve assumptions about the EL i.e.:

- $\Delta h = h_1 - h_0 = \text{Constant}$ (Betts 1974)
- $\Delta h = h_1 - h_0$ is related to the zero-order jump at h by two right angled

triangles with opposite sides of lengths $h_1 - h$ and $h - h_0$ (Batchvarova and Gryning 1994)

- Δh or maximum overshoot distance $d \propto \frac{w^*}{N}$ where w^* is the convective vertical velocity scale and $N = \sqrt{\frac{g}{\theta} \frac{\partial \theta}{\partial z}}$ is the Brunt-Vaisala frequency (Stull 1973)
- For $h_0 < z < h_1$ $\bar{\theta} = \bar{\theta}_{ML} + f(z, t)\Delta\theta$ where $f(z, t)$ is a dimensionless shape factor (Deardorff 1979, Federovich et al. 2004)

Although development of these models is beyond the scope of this thesis, they are mentioned to give context to the parameterizations considered in Sections 1.2.6 and 1.2.6.

Numerical Simulations

Numerical simulation of the CBL is carried out by solving the Navier Stokes equations, simplified according to a suitable approximation, on a discrete grid. Types of simulations can be grouped according to the scales of motion they resolve. In direct numerical simulations (DNS) the full range of spatial and temporal turbulence are resolved from the size of the domain down to the smallest dissipative scales i.e. the Kolmogorov micro-scales (Kolmogorov 1962). This requires a dense numerical grid and so can be computationally prohibitive.

In an LES motion on scales smaller than the grid spacing are filtered out and parameterized by a sub-grid scale closure model. General circulation models (GCM) solve the Navier Stokes equations on a spherical grid and parameterize smaller scale processes including convection and cloud cover. LES has increasingly been used to better understand the CBL since Dear-dorff (1972) applied this relatively new method for this purpose. Sullivan et al. (1998), Federovich et al. (2004) and Brooks and Fowler in (2012) used it to study the structure and scaling behaviour of the EL.

1.2.6 Scales and Scaling Relations of the CBL and EL

Length Scale (h)

Deardorff (1972) demonstrated that dominant turbulent structures in penetrative convection scale with CBL height, which he referred to as the inversion height but measured as the height of minimum average vertical heat flux: z_f as shown later in Figure 1.5 (Deardorff et al. 1980). Since then, the distinction between the two has been clarified (see Section 1.2.2) and here h refers strictly to the height of maximum average potential temperature gradient. There are alternatives. For example turbulence based definitions, such as the velocity variance and the distance over which velocity is correlated with itself, represent the current turbulent dynamics rather than the recent turbulence history as does h (Traumner et al. 2011).

Convective Velocity Scale (w^*)

Given an average surface vertical heat flux $(\overline{w'\theta'})_s$ a surface buoyancy flux can be defined as $\frac{g}{\theta}(\overline{w'\theta'})_s$ which gives the convective velocity scale when multiplied by the appropriate length scale. Since the result has units $\frac{m^3}{s^3}$ a cube root is applied

$$w^* = \left(\frac{gh}{\overline{\theta}} (\overline{w'\theta'})_s \right)^{\frac{1}{3}}. \quad (1.6)$$

Deardorff (1970) confirmed that this effectively scaled the local vertical turbulent velocity fluctuations (w') in the CBL. Sorbjan's (1996) work supports this, even at the CBL top. The CBL entrainment rate ($w_e = \frac{dh}{dt}$) depends on the magnitude of w' which is driven by $(\overline{w'\theta'})_s$. Stability aloft suppresses $\frac{dh}{dt}$ so the influence of γ is indirectly accounted for via h in w^* .

Convective Time Scale (τ)

It follows that the time a thermal, travelling at velocity scaled by w^* , takes to reach the top of the CBL i.e. travel a distance h is scaled by

$$\tau = \frac{h}{\left(\frac{gh}{\theta} (\overline{w'\theta'})_s\right)^{\frac{1}{3}}}. \quad (1.7)$$

This is also referred to as the convective overturn time scale. Sullivan et al. (1998) showed a linear relationship between h and time scaled by τ . An alternative is the Brunt-Vaisala frequency i.e. the time scale associated with the buoyant thermals overshooting and sinking (Federovich et al. 2004). The ratio of these two time-scales forms a parameter which characterizes this system (see Sorbjan 1996 and Deardorff 1979).

Temperature Scale (θ^*)

The CBL temperature fluctuations θ' are influenced by $\overline{w'\theta'}$ from both the surface and the CBL top. Deardorff (1970) showed that an effective scale based on the convective velocity scale is

$$\theta^* = \frac{(\overline{w'\theta'})_s}{w^*}. \quad (1.8)$$

Whereas Sorbjan (1996) showed that with proximity to the CBL top the effects of FA stability γ become more important.

Buoyancy Richardson Number (Ri)

The flux Richardson (R_f) number expresses the balance between mechanical and buoyant production of turbulent kinetic energy (TKE) and is obtained from the ratio of these two terms in the TKE budget equation (See Appendix, Stull 1988):

$$R_f = \frac{\frac{g}{\theta} (\overline{w'\theta'})_s}{u_i u_j \frac{\partial \bar{U}_i}{\partial x_j}}. \quad (1.9)$$

Assuming horizontal homogeneity and vertically constant subsidence yields

$$R_f = \frac{\frac{g}{\theta} \left(\overline{w' \theta'} \right)}{\overline{u' w'} \frac{\partial \bar{U}}{\partial z} + \overline{v' w'} \frac{\partial \bar{V}}{\partial z}}. \quad (1.10)$$

Applying first order closure to the flux terms, i.e. assuming they are proportional to the vertical gradients, gives the gradient Richardson number (R_g)

$$R_g = \frac{\frac{g}{\theta} \frac{\partial \bar{\theta}}{\partial z}}{\left(\frac{\partial \bar{U}}{\partial z} \right)^2 + \left(\frac{\partial \bar{V}}{\partial z} \right)^2}, \quad (1.11)$$

However, in the EL buoyancy acts to suppress buoyant production of TKE. Applying a bulk approximation to the denominator, and expressing it in terms of scales yields a squared ratio of two time scales

$$R_g = \frac{\frac{g}{\theta} \frac{\partial \bar{\theta}}{\partial z}}{\frac{U^{*2}}{L^2}} = N^2 \frac{L^2}{U^{*2}}, \quad (1.12)$$

where U^* and L^* are appropriate velocity and length scales. Applying the bulk approximation to both the numerator and denominator yields the bulk Richardson number:

$$R_b = \frac{\frac{g}{\theta} \Delta \theta L^*}{U^{*2}}. \quad (1.13)$$

A natural choice of length and velocity scales for the CBL are h and w^* giving the convective or buoyancy Richardson number:

$$Ri = \frac{\frac{g}{\theta} \Delta \theta h}{w^{*2}}. \quad (1.14)$$

Where $\Delta \theta$ can be replaced by $\delta \theta$ as in Federovich et al. (2004) and Garcia and Mellado (2014). Ri can also be arrived at by considering the principal forcings of the system, or from non-dimensionalizing the entrainment relation derived analytically (Tennekes 1973, Deardorff 1972). It is central to any study on CBL entrainment (Sullivan et al. 1998, Federovich et al. 2004, Traumner et al. 2011, Brooks and Fowler 2012).

Relationship of Entrainment Layer Depth to Richardson Number

A relationship of the scaled entrainment layer EL depth to Ri

$$\frac{\Delta h}{h} \propto Ri^b \quad (1.15)$$

is arrived at by considering the deceleration of a thermal as it overshoots its neutral buoyancy level (Nelson et al. 1989). If the velocity of the thermal is assumed to be proportional to w^* and the decelerating force is due to the buoyancy difference, or θ jump, then the distance the thermal overshoots (d) can be approximated by

$$d \propto \frac{w^{*2}}{\frac{g}{\bar{\theta}_{ML}} \Delta \theta}. \quad (1.16)$$

If the EL depth is proportional to the overshoot distance (d) then

$$\frac{\Delta h}{h} \propto \frac{w^{*2}}{\frac{g}{\bar{\theta}_{ML}} \Delta \theta h} = Ri^{-1}. \quad (1.17)$$

Alternatively, Boers 1989 integrated the internal (U), potential (P) and kinetic (K) energy over a hydrostatic atmosphere

$$U = \frac{c_v}{g} \int_0^{p_0} T dp. \quad (1.18)$$

$$P = \frac{R}{c_v} U, \quad (1.19)$$

and

$$K = \frac{1}{2} \int_0^{p_0} \frac{w^2}{g} dp. \quad (1.20)$$

p_0 is the surface pressure, R and c_v are the gas constant and heat capacity of dry air at constant volume. T is temperature. Initially there is a flat infinitesimally thin inversion interface which is distorted by an impinging thermal. The resulting height difference is assumed sinusoidal and an average Δh is obtained by integrating over a wavelength. At this point, no

entrainment is assumed to have occurred and all of the initial kinetic energy (K_i) has been transferred to the change in potential energy (ΔP).

$$K_i = P_f - P_i = \Delta P \quad (1.21)$$

Assuming a dry adiabatic atmosphere and that the vertical velocity in the layer below the inversion can be approximated by the convective velocity scale (w^*), the following expression is reached

$$\left(\frac{\Delta h}{h}\right)^2 \propto \frac{T_0 w^{*2}}{g \Delta \theta h}. \quad (1.22)$$

The reference temperature, T_0 , can be replaced by $\bar{\theta}_{ML}$ to give

$$\frac{\Delta h}{h} \propto Ri^{-\frac{1}{2}} \quad (1.23)$$

Relationship of Entrainment Rate to Richardson Number

The relationship between scaled entrainment rate and the buoyancy Richardson number (Ri)

$$\frac{w_e}{w^*} \propto Ri^a \quad (1.24)$$

is arrived at according to the zero order bulk model through thermodynamic arguments, or by integration of the conservation of enthalpy or turbulent kinetic energy equations over the growing CBL. (Tennekes 1973, Deardorff 1979, Federovich et al. 2004). It has been verified in numerous laboratory and numerical studies (Deardorff et al. 1980, Sullivan et al. 1998, Federovich et al. 2004, Brooks and Fowler 2012), but there is still some unresolved discussion as to the exact value of a . It seems there are two possible values, $-\frac{3}{2}$ and -1 , the first of which Turner (1986) suggested occurs at high stability when buoyant recoil of impinging thermals becomes more important than their convective overturning. Assume that an impinging thermal supplies kinetic energy (K) per unit time and per unit area for entrainment, in terms of appropriate length and time scales L^* and t^* as follows

$$K \propto \frac{\bar{\rho} L^{*3} U^{*2}}{L^{*2} t^{*}}, \quad (1.25)$$

and that the corresponding change in potential energy per unit time and area of the rising CBL is

$$\Delta P \propto g \Delta \theta h \frac{dh}{dt} \quad (1.26)$$

where $\Delta\theta$ can be replaced with $\delta\theta$. If L^* is the penetration depth of the thermals travelling at velocity scaled by w^* against a decelerating force $g \frac{\Delta\theta}{\bar{\theta}}$

$$L^* = \frac{w^{*2} \bar{\theta}}{\Delta\theta}. \quad (1.27)$$

and t^* is the response time of the inversion layer to a thermal of length h

$$t^* = \sqrt{h \frac{\bar{\theta}}{g \Delta\theta}} \quad (1.28)$$

then assuming all of K is transferred to the change in potential energy (ΔP) and using the covective velocity scaled, yields

$$\frac{dh}{dt} \propto \frac{\bar{\theta} w^{*2}}{g \Delta\theta h} \sqrt{\frac{\bar{\theta} w^{*2}}{g \Delta\theta h}}, \quad (1.29)$$

i.e.

$$\frac{w_e}{w^*} \propto Ri^{-\frac{3}{2}}. \quad (1.30)$$

Adding further complexity to this discussion, Federovich et al. (2004) suggest that this power law relationship ($a = -\frac{3}{2}$) can be arrived at through defining the θ jump across the EL rather than at h (see Figure 1.3).

1.3 Research Questions

A simplified conceptual model of the dry, shear-free CBL in the absence of large scale winds is represented in Figure 1.3. The two principal external

parameters in this case, are the average vertical turbulent surface heat flux ($\overline{w'\theta'}$)_s and the upper lapse rate (γ) (Federovich et al. 2004, Sorbjan 1996). They have opposing effects, that is to say ($\overline{w'\theta'}$)_s drives upward turbulent velocity (w'^+) and so CBL growth (w_e) whereas γ suppresses it. Conversely they both cause positive turbulent potential temperature fluctuations (θ'^+) and so warming of the CBL. In the EL the thermals from the surface are now relatively cool. They turn downwards as they interact with the stable FA concurrently bringing down warmer air. Sullivan et al. (1998) demonstrated these dynamics by partitioning $\overline{w'\theta'}$ into four quadrants. Sorbjan (1996) asserted and showed that in this region the turbulent potential temperature fluctuations (θ') are strongly influenced by γ whereas the turbulent vertical velocity fluctuations (w') are almost independent thereof. Inspired by these two studies and to gain some insight into the dynamics of this idealized CBL I ask **Q1: How do the distributions of local CBL height, and the joint distributions of w' and θ' within the EL, vary with $(\overline{w'\theta'})_s$ and γ ?**

The relationship between scaled EL depth and Ri

$$\frac{\Delta h}{h} \propto Ri^b \quad (1.15)$$

has been explored and justified in field measurement, laboratory and numerical studies. There is disagreement with respect to its exact form, in part stemming from variation in height and θ jump definitions, but in general its magnitude relative to h decreases with increasing Ri . Although referred to in most relevant studies and relied upon in analytical models, the vertical average potential temperature profile has not been used to define the EL (Deardorff et al. 1980, Nelson et al. 1989, Federovich et al. 2004, Boers 1989, Brooks and Fowler 2012). This leads me to ask **Q2: Can the EL limits be defined based on the $\bar{\theta}$ profile and what is the relationship of the resulting depth (Δh) to Ri ?**

A further simplification to the dry, shear-free, CBL model without large

scale velocities, is to regard the EL depth as infinitesimally small as in Figure 1.4. The relationship of the scaled, time rate of change of h (entrainment rate: w_e) to Ri can be derived based on this model (Tennekes 1973, Deardorff 1979, Federovich et al. 2004)

$$\frac{w_e}{w^*} \propto Ri^a. \quad (1.24)$$

This will be referred to as the entrainment relation. Although such a relationship is well established, discussion as to the power exponent of Ri is unresolved and results from studies justify values of both $-\frac{3}{2}$ and -1 . See Traumner et al. (2011) for a summary and review. Turner (1986) explains this disparity in terms of entrainment mechanism such that the higher value occurs when thermals recoil rather than overturn in response to a stronger θ jump (or inversion). Whereas Sullivan et al. (1998) notice a deviation from the lower power (-1) at lower Ri and attribute it to the effect of the shape of $\bar{\theta}$ within a thicker EL. Both Federovich et al. (2004) and Garcia and Mellado (2014) show how the definition of the θ jump influences the time rate of change of Ri and so effects a . **Q3: How does defining the θ jump based on the vertical $\bar{\theta}$ profile across the EL as in Figure 1.3 vs at the inversion (h) as in Figure 1.4, affect the entrainment relation and in particular a ?**

1.4 Approach to Research Questions

General Setup

I modelled the dry shear free CBL and EL using LES, specifically the cloud resolving model System for Atmospheric Modelling (SAM) to be outlined in Chapter 3. An ensemble of 10 cases was run to obtain true ensemble averages and turbulent potential temperature variances (θ'), each case had a domain of area $3.2 \times 4.8 \text{ Km}^2$. Grid spacing was influenced by the resolution study of Sullivan and Patton (2011) and the vertical grid within the EL was of higher resolution than that applied in other comparable work. The runs

were initialized with a constant $(\overline{w'\theta'})_s$ acting against a uniform γ . So, the θ jump arose from the overshoot of the thermals, rather than being initially imposed as in Sullivan et al. (1998) and Brooks and Fowler (2012).

Verifying Output

Before addressing the questions stated in Section 1.3 I will examine the modeled output to make sure it represents a realistic turbulent CBL in Chapter 3 section 2. I will verify that the averaged vertical profiles are as expected and coherent thermals are being produced. FFT energy density spectra will show if there is adequate scale separation between the structures of greatest energy and the grid spacing, and that realistic, isotropic turbulence is being modelled.

Q1

The EL can be thought of in terms of the distribution of individual thermal heights, or local heights. Sullivan et al. (1998) measured local height by locating the vertical point of maximum θ gradient, and observed the effects of varying Ri on the resulting distributions. However this method is problematic when gradients in the upper profile exceed that at the inversion (Brooks and Fowler 2012). Steyn et al. (1999) fitted an idealized curve to a lidar backscatter profile. This method produces a smooth curve based on the full original profile on which a maximum can easily be located. I will apply a multi-linear regression method outlined in Vieth (2011) to the local θ profile, representing the ML, EL and FA each with a separate line segment. From this fit, I will locate the ML top (h_0^l). I'll observe how the resulting distributions are effected by changes in $(\overline{w'\theta'})_s$ and γ using histograms in Chapter 3 Section 3.

Sullivan et al. (1998) broke the turbulent vertical heat flux $w'\theta'$ into four quadrants and used this combined with local flow visualizations to show how CBL thermals impinge and draw down warm air from above. Mahrt

and Paumier (1984) used 2 dimensional contour plots of local w' and θ' measurements to analyze their joint distributions. In his 1996 LES study Sorbjan showed that in the EL, θ' is strongly influenced by γ whereas w' is independent thereof. Influenced by these three studies, I will use 2 dimensional histograms at h and so within the EL to look at how the distributions of local w' and θ' are effected by changes in γ and $(\overline{w'\theta'})_s$. I will magnify the effects of γ , by applying the convective scales, θ^* and w^* and hone in specifically on the entrained air at h in Chapter 3 Section 4.

Q2

Here I define the CBL height as the location of maximum vertical $\bar{\theta}$ gradient as in Figure 1.5. The lower and upper EL limits are then the points at which $\frac{\partial \bar{\theta}}{\partial z}$ significantly exceeds zero and where it resumes γ . The lower limit requires choice of a threshold value which should be small, positive and less than γ . Since it is somewhat arbitrary I will compare results based on three different threshold values in Chapter 3 section 5. Federovich et al. (2004) and Brooks and Fowler (2012) defined the EL in terms of the vertical $\overline{w'\theta'}$ profiles as in Figure 1.5 but disagreed on the shape of the relationship of scaled EL depth to Ri (equation 2.1). As well as observing this relationship using the height definitions based on the $\bar{\theta}$ profile, I will apply the definitions based on the $\overline{w'\theta'}$ profile for comparison with Brooks and Fowler (2012) and Federovich et al. (2004) in Chapter 3 section 4.

CBL Height	ML $\bar{\theta}$	θ Jump	Ri
h	$\bar{\theta}_{ML} = \frac{1}{h} \int_0^h \bar{\theta}(z) dz$	$\Delta\theta = \bar{\theta}(h_1) - \bar{\theta}(h_0)$ $\delta\theta = \bar{\theta}_0(h) - \bar{\theta}_{ML}$	$Ri_\Delta = \frac{\frac{g}{\bar{\theta}_{ML}} \Delta\theta h}{w^{*2}}$ $Ri_\delta = \frac{\frac{g}{\bar{\theta}_{ML}} \delta\theta h}{w^{*2}}$

Table 1.1: Definitions based on the vertical $\bar{\theta}$ profile in Figure 1.5. To obtain those based on the $\overline{w'\theta'}$ profile, replace h_0 , h and h_0 with z_{f0} , z_f and z_{f1}

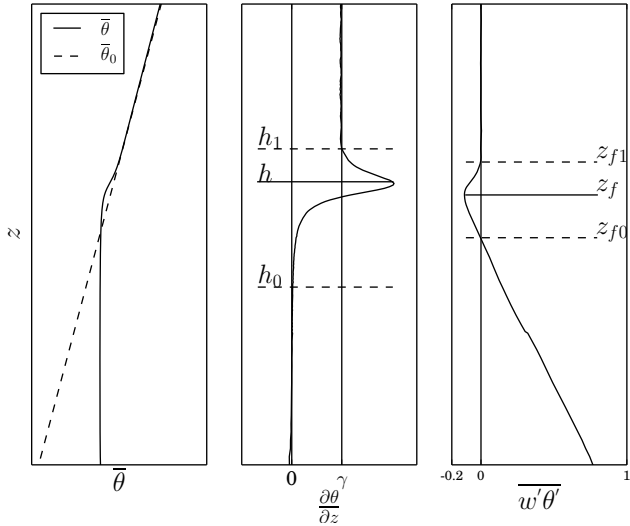


Figure 1.5: Height definitions based on the average vertical profiles.
 θ_0 is the initial potential temperature.

Q3

As discussed in see Section 1.2.6 the form of the entrainment relation is thought to vary based on the mechanism that initiates entrainment, which in turn depends on the magnitude of Ri . Furthermore the ways in which the height and θ jump are defined have an effect. I will vary the definition of the θ jump as outlined in table 2.2 in order to discern between how this, and variation in initial conditions, influence the entrainment relation and in particular a . I will reproduce this analysis using height definitions based on $\overline{w' \theta'}$ for comparison with the results of Federovich et al. (2004).

2. Research Questions Answered using Model Output

In Section 2.1 vertical profiles of the ensemble and horizontally averaged potential temperature and heat flux ($\bar{\theta}$ and $\overline{w'\theta'}$) will be checked for the development of the expected three layer structure (ML, EL and FA). In order to verify that there is sufficient scale separation and so an adequate inertial subrange, FFT energy spectra of the turbulent velocity fluctuations will be plotted. To convince the reader (and myself) that multiple coherent thermals are being produced, 2 dimensional visualizations will be shown at the three heights: h_0 , h and h_1 as shown in Figure 1.5.

Section 2.2 will focus on answering **Q1**:

How do the distributions of local CBL height, and the joint distributions of w' and θ' within the EL, vary with $(\overline{w'\theta'})_s$ and γ ?

The distributions of local ML heights at each horizontal point, in each ensemble member, will be plotted as histograms to visualize the effects of $(\overline{w'\theta'})_s$ and γ . For the same reason the joint distributions of local potential temperature and velocity fluctuations (θ' and w') at h will be plotted. Focus will then be narrowed to the average downward moving warm quadrant at h ($\overline{(w'-\theta')^+}_h$, $\overline{w'}^-_h$ where $\theta' > 0$ and $\overline{\theta'}^+_h$ where $w' < 0$) to examine the direct influence of γ on entrainment.

To answer **Q2**:

Can the EL limits be defined based on the $\bar{\theta}$ profile and what is the relationship

$$\frac{\Delta h}{h} \propto Ri^b \quad (1.15)$$

of the resulting depth (Δh) to Ri ?

in Section 2.3, Equation 1.15 will be plotted using height definitions based on the $\frac{\partial \bar{\theta}}{\partial z}$ profile as in Figure 1.5 and Table 2.2. Since the choice of a threshold to determine the lower EL limit is somewhat arbitrary, plots will be reproduced using two additional values. For comparison with the results of Federovich et al. (2004) and Brooks and Fowler (2012), Equation 1.15 will be plotted using heights based on the average heat flux ($\bar{w}'\bar{\theta}'$) profile.

In Section 2.4 the temperature jump will be defined in four ways to answer
Q3: How does defining the θ jump based on the vertical $\bar{\theta}$ profile across the EL as in Figure 1.3 vs at the inversion (h) as in Figure 1.4, affect the entrainment relation

$$\frac{w_e}{w^*} \propto Ri^a \quad (1.24)$$

and in particular a ?

For a more detailed discussion refer to Section 1.4. This analysis will involve a look at how the heights evolve in time and culminate in four plots representing Equation 1.24 in log-log coordinates such that the most suitable values of the exponent a can be seen.

2.1 Verifying the Model Output

2.1.1 Initialization and Spin-Up Time

All 10 member cases of the ensemble were carried out on a 3.2 x 4.8 Km horizontal domain ($\Delta x = \Delta y = 25m$, $nx = 128$, $ny = 192$). Grid numbers nx , ny were chosen based on the optimal distribution across processor nodes. The vertical grid ($nz = 312$) was of higher resolution around the entrainment layer ($\Delta z = 5m$), lower below ($\Delta z = 25m$) and stretched above it ($\Delta z = 10$ to $100m$). This was guided by Sullivan and Patton's 2011 LES resolution study of the CBL that showed how grid size effects; the shapes of the average vertical profiles in particular around the EL, as well as the extent of the inertial sub-range. The 7 runs, summarized in Table 2.1, are all initialized with a constant surface heat flux ($(\overline{w'\theta'_s})_s$) acting against a uniform initial lapse rate (γ) and differ from each other based on these two external parameters.

$\overline{w'\theta'_s} / \gamma$	10 (K/Km)	5 (K/Km)	2.5 (K/Km)
150 (W/m ²)	✓	✓ ¹	
100 (W/m ²)	✓	✓	
60 (W/m ²)	✓	✓	✓

Table 2.1: Runs in terms of $\overline{w'\theta'_s}$ and initial lapse rate γ

Time must be allowed to establish statistically steady turbulent flow. Sullivan et al. (1998) recommended 10 eddy turnover times based on the convective time scale $\tau = \frac{h}{w^*} = \frac{h}{\left(\frac{gh}{\theta_{ML}}(\overline{w'\theta'_s})\right)^{\frac{1}{3}}}$, and Brooks and Fowler (2012) chose a simulated time of 2 hours. Figure 2.1 shows that for all of the runs, at least 10 eddy turnover times were completed by 2 simulated hours. Although each run has a distinct convective velocity scale w^* , that increases with time, dividing boundary layer height, h , by it to obtain τ results in a

¹Incomplete run: EL exceeded high resolution vertical grid after 7 hours

collapse from 7 to 3 curves, one for each γ .

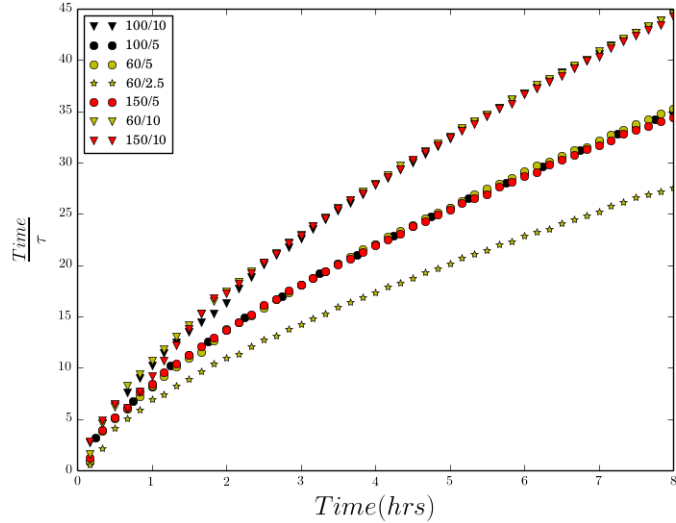


Figure 2.1: Plots of scaled time vs time for all runs. Scaled time is based on the convective time scale τ and can be thought of as the number of times an eddy has reached the top of the CBL.

Figure 2.2 shows that by two hours there is a measurable well mixed layer (ML) where: (i) the horizontally and ensemble averaged potential temperature ($\bar{\theta}$) is constant, (ii) its vertical gradient $\frac{\partial \bar{\theta}}{\partial z}$ is close to zero and (iii) the average heat flux $\overline{w'\theta'}$ is positive and linearly decreasing. Above it is an EL where the vertical $\bar{\theta}$ profile transitions through a maximum to the upper lapse rate γ and $\overline{w'\theta'}$ is negative. By 3 hours the EL is fully contained within the vertical region of high resolution in all runs. Figure 2.3 shows that the $\overline{w'\theta'}$ profiles are similar and are scaled well by the surface heat flux ($(\overline{w'\theta'})_s$) by 2 hours.

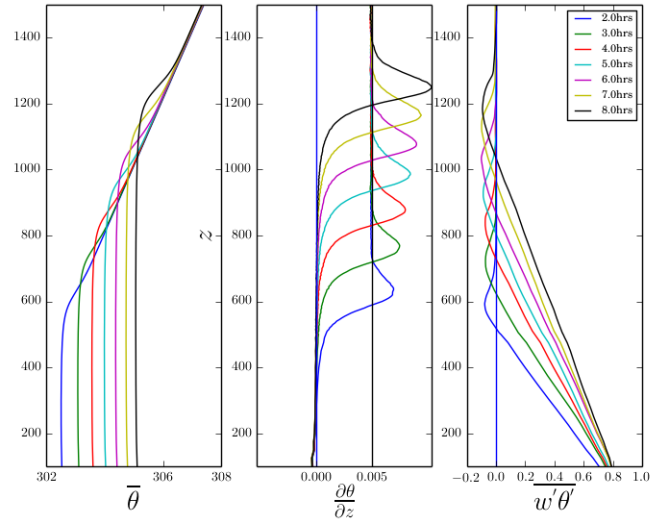


Figure 2.2: Vertical profiles of the horizontally and ensemble averaged potential temperature ($\bar{\theta}$), its vertical gradient ($\frac{\partial \bar{\theta}}{\partial z}$) and heat flux ($\overline{w'\theta'}$) for the 100/5 run

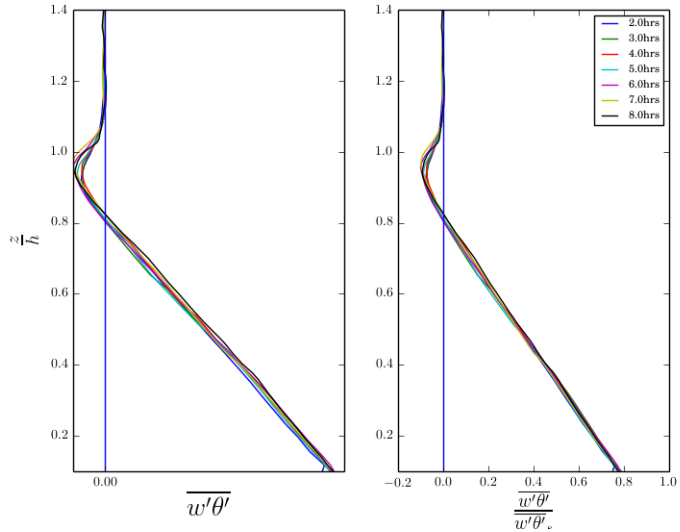


Figure 2.3: $\overline{w'\theta'}$ and scaled $\overline{w'\theta'}$ vs scaled height for the 100/5 run

2.1.2 Horizontally and Ensemble averaged vertical Potential Temperature $\bar{\theta}$ and Heat Flux $\overline{w'\theta'}$ Profiles

In Figures 2.2 and 2.4 the $\bar{\theta}$ profiles exhibit an ML above which $\frac{\partial \bar{\theta}}{\partial z} > 0$ and reaches a maximum value at h before resuming γ at h_1 . Convective boundary layer CBL growth is stimulated by $(\overline{w'\theta'})_s$ and inhibited by γ .

In Figures 2.2 and 2.5 the $\overline{w'\theta'}$ profiles decrease from the surface value, $(\overline{w'\theta'})_s$, passing through zero to a minimum before increasing to zero. They are similar across runs when scaled by $(\overline{w'\theta'})_s$. All minima are less in magnitude than the zero order approximation, $-.2 \times (\overline{w'\theta'})_s$ (Tennekes 1973), but seem to increase with increased γ .

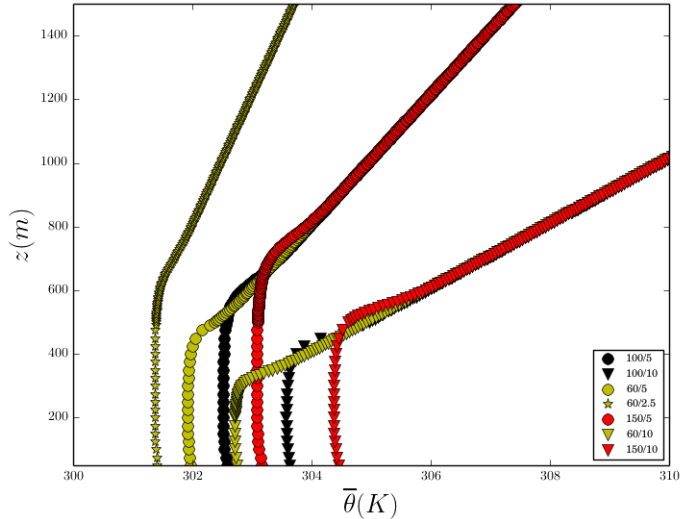


Figure 2.4: $\bar{\theta}$ profiles at 2 hours for all runs

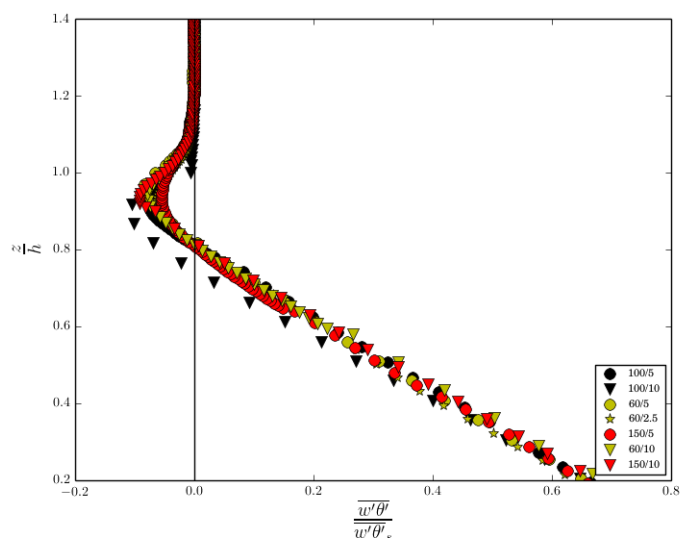


Figure 2.5: Scaled $(\overline{w'\theta'})_s$ profiles at 2 hours for all runs

2.1.3 FFT Energy Spectra

In Figure 2.6, two dimensional FFT power spectra taken of horizontal slices of w' at three different levels (h_0 , h and h_1 as shown in Figure 1.5) are collapsed to one dimension by integrating around a semi-circle of positive wave-numbers. Isotropy in all radial directions is assumed and $k = \sqrt{k_x^2 + k_y^2}$. The resulting scalar density spectra show peaks in energy at the larger scales, cascading to the lower scales roughly according to a $-\frac{5}{3}$ slope lower in the EL. At the top of the EL where turbulence is suppressed by stability, the slope is steeper. The peak in energy occurs at smaller scales at h as compared to at h_0 , indicating a change in the size of the dominant turbulent structures. The spectra for the horizontal turbulent velocity fluctuations were analogous but show lower energy as expected. All runs produced spectra with these characteristics.

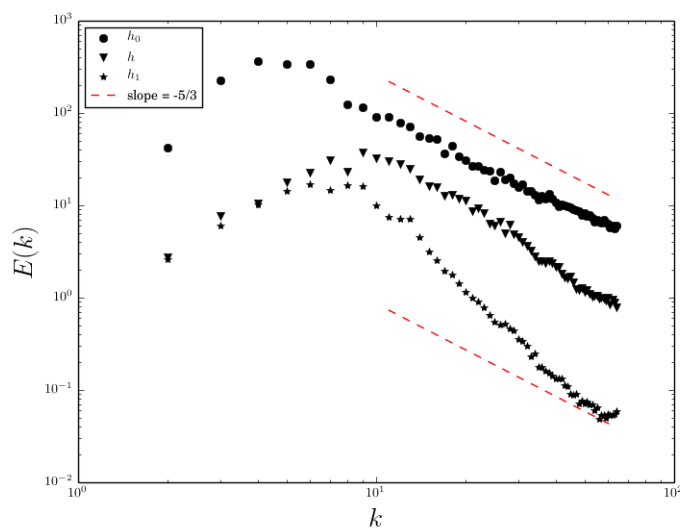


Figure 2.6: Scalar FFT energy vs wavenumber ($k = \sqrt{k_x^2 + k_y^2}$) for the 60/2.5 run at 2 hours. $E(k)$ is $E(k_x, k_y)$ integrated around circles of radius k . $E(k_x, k_y)$ is the total integrated energy over the 2D domain. k_x and k_y are number of waves per domain length.

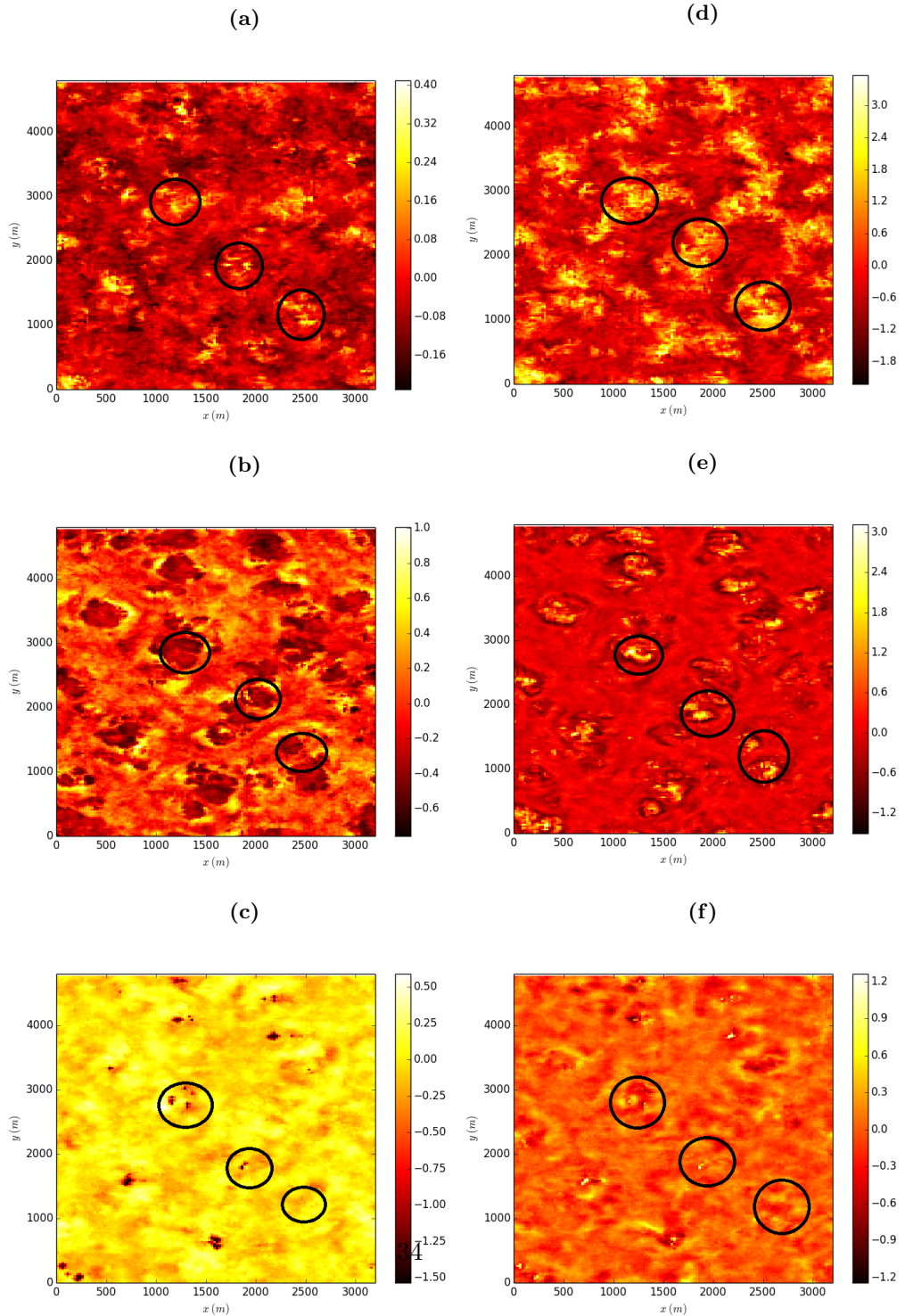
2.1.4 Visualization of Structures Within the Entrainment Layer

Horizontal slices, at h_0 , h and h_1 as shown in Figure 1.5 of the potential temperature and vertical velocity fluctuations are plotted to see the turbulent structures. Figure 2.7 shows the bottom of the EL (h_0) for the 150/10 run where coherent areas of positive and negative temperature fluctuations correspond to areas of upward and downward moving air. In (b) and (e) the individual thermals of relatively cool air are more evident at the inversion (h) and their locations correspond to areas of upward motion. Most of the upward moving cool areas are adjacent to and even encircled by smaller areas of downward moving warm air. At h_1 ((c) and (f)) peaks of cool air are associated with both up and down-welling.

2.1.5 Summary of Findings

Each 10 member ensemble run was allowed a period of time to develop the three layer structure (ML, EL and FA) as seen from the vertical average potential temperature ($\bar{\theta}$) and vertical turbulent heat flux ($\bar{w'\theta'}$) profiles. The convective time scale (τ) for a thermal to reach the CBL top (h) was seen to depend on γ , signalling the importance of this external parameter. FFT spectra of turbulent velocity fluctuations the ML showed a satisfactory inertial subrange and several coherent impinging thermals were observed in the EL at any given time after 2 hours, indicating that realistic turbulence was being simulated.

Figure 2.7: θ' (left) and w' (right) at 2 hours at h_0 (a,d), h (b,e) and h_1 (d,f) for the 150/10 run.



2.2 Local Statistics (Q1)

2.2.1 Local Mixed Layer Heights (h_0^l)

In Figures 2.8 and 2.9 the local vertical θ profiles, each at a single horizontal point in an individual case, exhibit a distinct ML before resuming γ but not always a clearly defined EL. There are sharp changes in the profile well into the free atmosphere, due possibly to waves, which render the gradient method for determining a local CBL height, h^l , unusable. Instead a linear regression method is used, whereby three lines representing: the ML, the EL and the upper lapse rate (γ), are fit to the profile according to the minimum residual sum of squares. Determining local ML height (h_0^l) in this way was more straight forward than the local height of maximum potential temperature gradient (h^l) for the reasons stated above.

Figure 2.8 shows two local θ profiles where h_0^l is relatively high. A sharp interface is evident indicating that this is within an active thermal impinging on the stable layer. In Figure 2.9 where h_0^l is relatively low a less defined interface indicates a point now outside a rising thermal. When γ is lower in magnitude as in Figure 2.9 (a), these inactive locations show a larger vertical region that could be called a local EL. In 2 dimensional horizontal plots, not shown here, regions of high h_0^l corresponded to regions of upward moving relatively cool air at h .

The distribution of h_0^l represents the range over which CBL height varies in space, so as discussed in Section 1.2.4, relates to the depth of the entrainment layer (EL). Figure 2.10 illustrates that the spread increases with increasing $(\overline{w'\theta'})_s$ and decreases with increasing γ . When scaled by h , as in Figure 2.11, the local ML height distribution narrows with increased γ and seems relatively uninfluenced by change in $(\overline{w'\theta'})_s$. The upper limit seems to be constant at about $1.1(\times h)$, whereas the lower limit increases with increased γ . Runs with lower h and narrower Δh have relatively larger spacing between bins and so higher numbers in each bin.

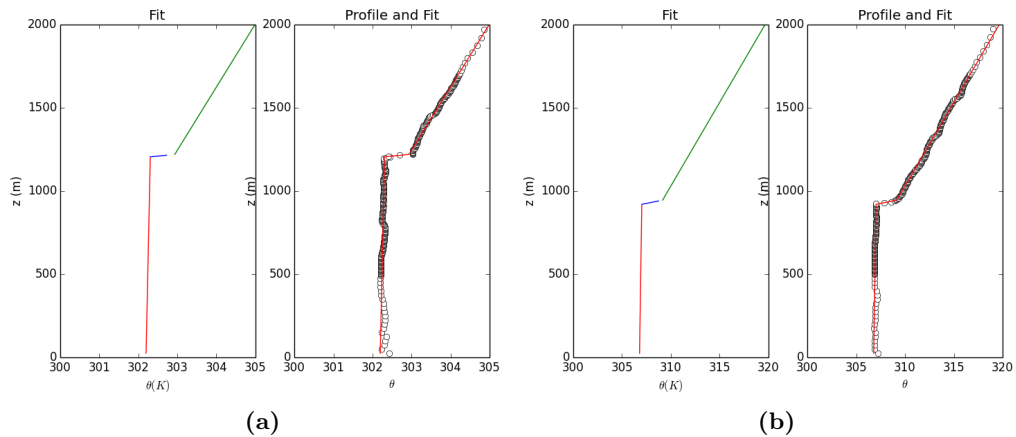


Figure 2.8: Local vertical θ profiles with 3-line fit for the 60/2.5 (a) and 150/10 (b) runs at points where h_0^l is high.

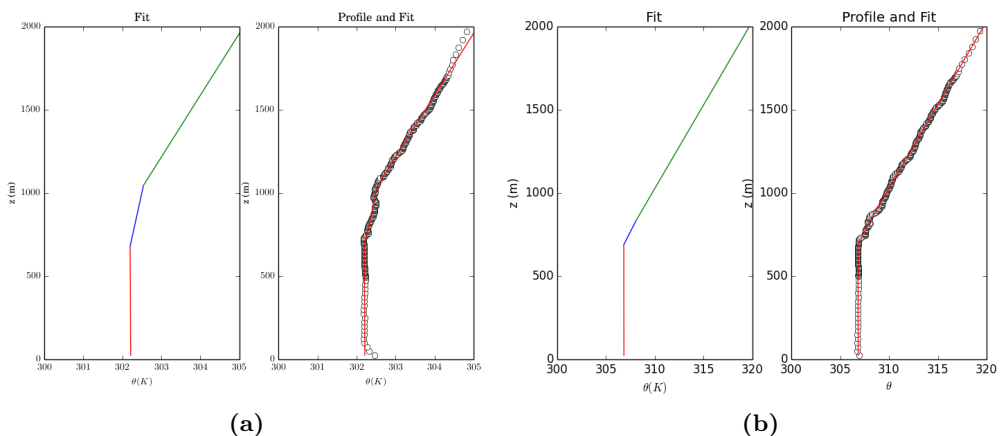


Figure 2.9: Local vertical θ profiles with 3-line fit for the 60/2.5 (a) and 150/10 (b) runs at points where h_0^l is low.

Figure 2.10: Histograms of h_0^l at each horizontal point in each ensemble case for $(w'\theta')_s = 150$ to $60(W/m^2)$ (a to c) and $\gamma = 10$ to $2.5(K/Km)$ (c to g) at 5 hours

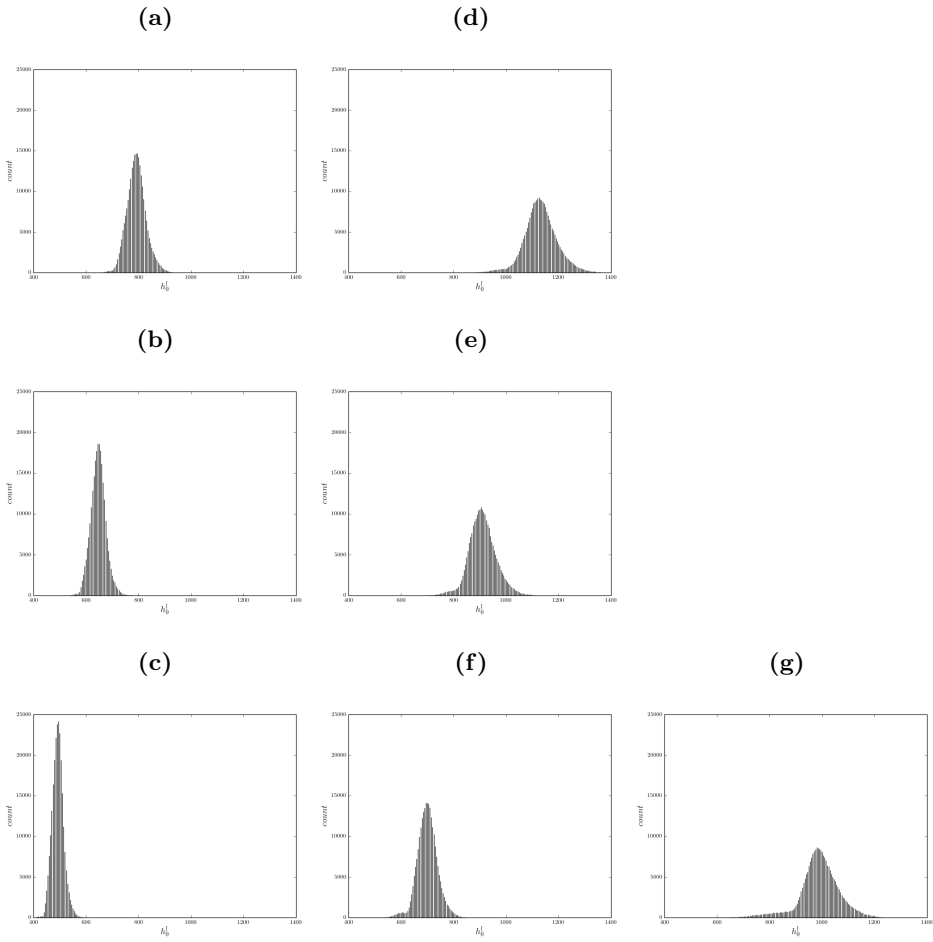
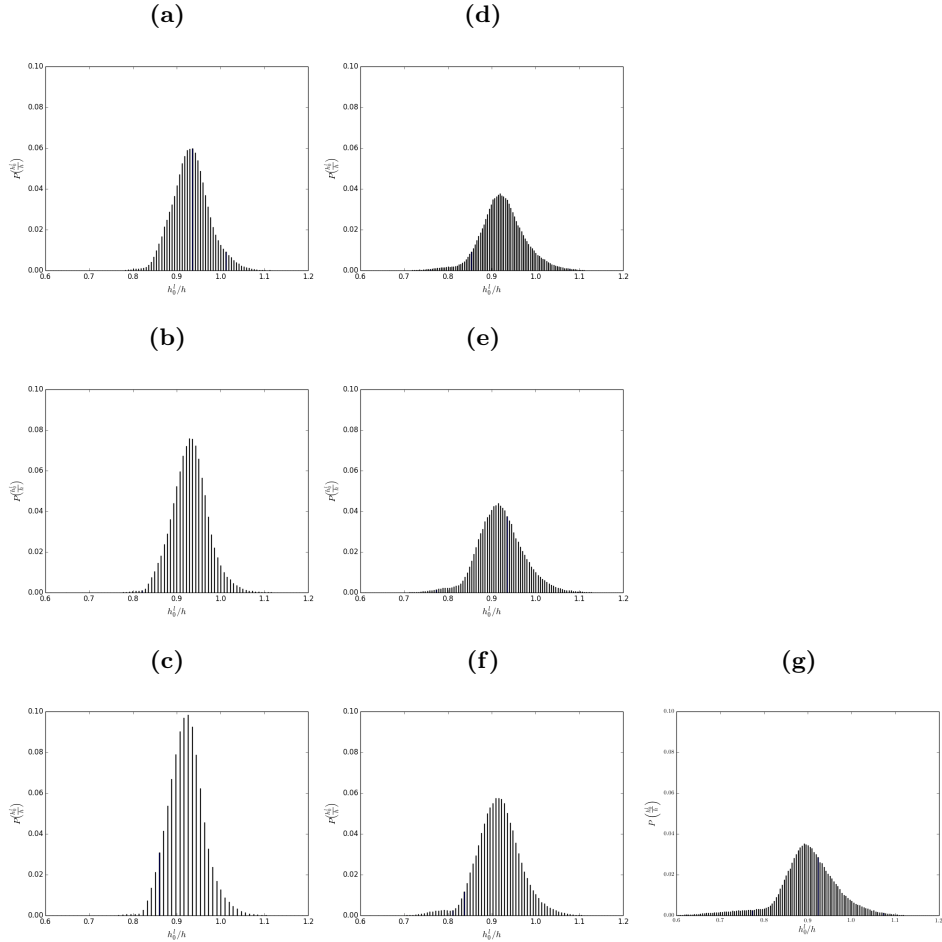


Figure 2.11: PDFs of $\frac{h_0^l}{h}$ for $(\overline{w'\theta'})_s = 150$ to $60(W/m^2)$ (top to bottom) and $\gamma = 10$ to $2.5(K/Km)$ (left to right) at 5 hours



2.2.2 Local turbulent Velocity and Potential Temperature Fluctuations

The 2 dimensional histograms of θ' and w' , at each horizontal point in each ensemble case, for all runs at h are plotted in Figure 2.12 to visualize how the distributions are influenced by changes in $(\overline{w'\theta'})_s$ and γ . In order to isolate the effects of γ , w' and θ' are scaled by w^* and θ^* respectively and plotted in Figure 2.13.

The spread of both w' and θ' increases with increasing $(\overline{w'\theta'})_s$ whereas that of θ' increases only slightly with increased stability (γ) in Figure 2.12. As expected, γ inhibits both upward and downward w' . The scaled version in Figure 2.13 shows a damping of the velocity fluctuations and a positive shift in temperature fluctuations with increased γ .

Although the quadrant of overall largest magnitude is that of upward moving cool air ($w'^+\theta'^-$), Sullivan et al.'s (1998) assertion that in the EL (i.e. at z_f) the net heat flux is downward moving warm ($w'^-\theta'^+$) air because the other three quadrants cancel, is found to be approximately true.

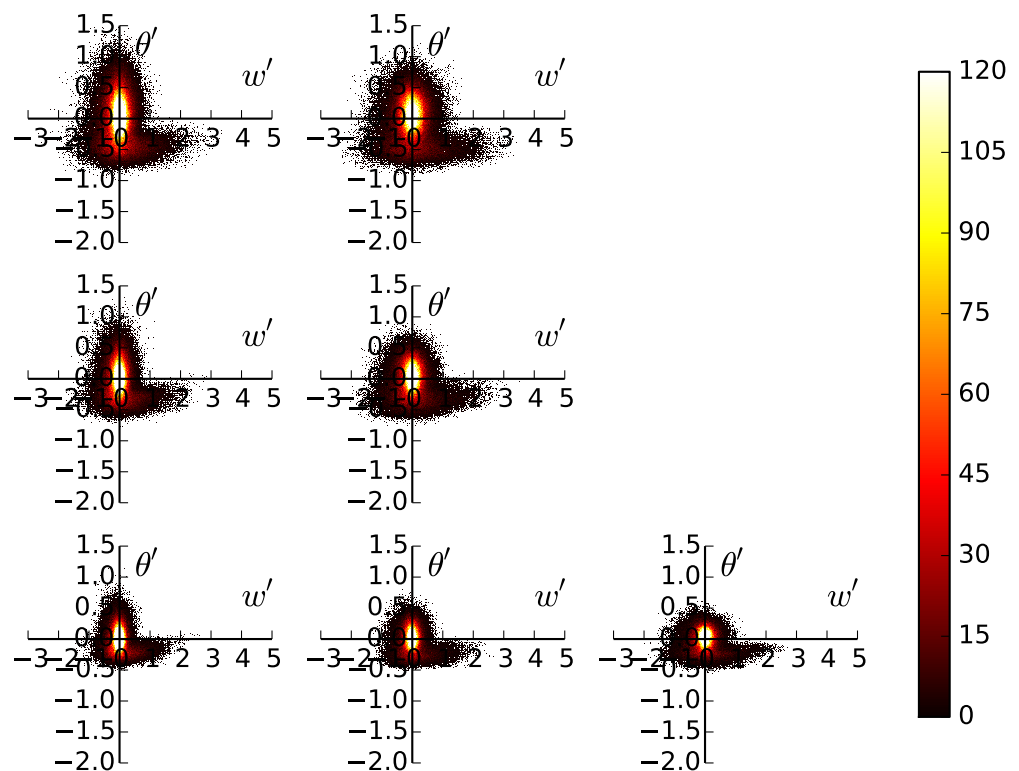


Figure 2.12: 2 dimensional histograms of w' and θ' at h for $w' \theta' = 150 - 60(\text{W}/\text{m}^2)$ (top - bottom) and $\gamma = 10 - 2.5(\text{K}/\text{Km})$ (left - right) at 5 hours

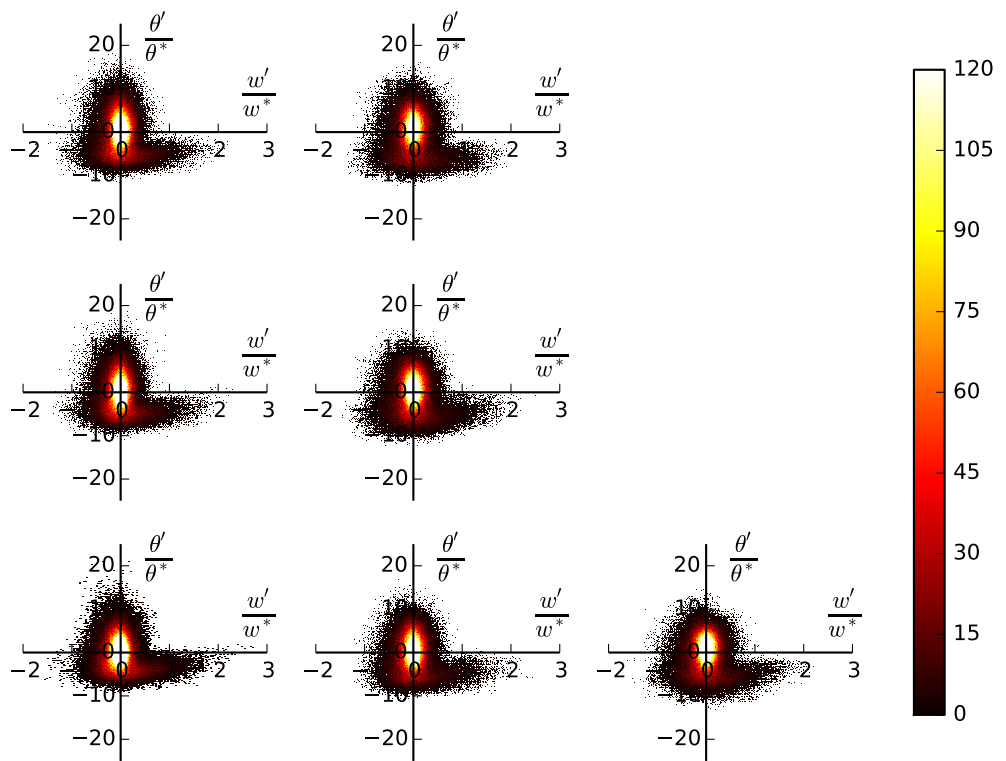


Figure 2.13: Scaled 2 dimensional distributions of w' and θ' at h for $(\overline{w'\theta'})_s = 150 - 60(\text{W}/\text{m}^2)$ (top - bottom) and $\gamma = 10 - 2.5(\text{K}/\text{Km})$ (left - right) at 5 hours

2.2.3 Downward Moving Warm Air at h

The average downward moving quadrant ($\overline{w' - \theta'^+}_h$) at h represents the pockets of trapped or engulfed warm air that become mixed into the growing CBL. So its magnitude can be taken as a measure of entrainment. Figure 2.14 shows that this increases in time as well as with increased $(\overline{w'\theta'})_s$. Grouping according to $(\overline{w'\theta'})_s$ is evident and there is further collapse when this is applied as scale in Figure 2.14 (b). Further partitioning $(\overline{w' - \theta'^+})_h$ into its velocity and temperature components reveals additional complexity.

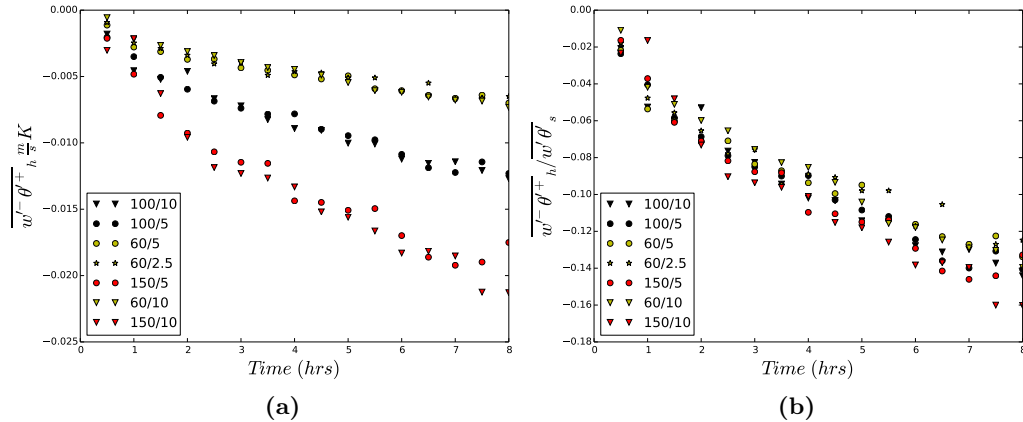


Figure 2.14: Plots of (a) the average downward moving warm air at h ($\overline{w' - \theta'^+}_h$) and (b) $\overline{w' - \theta'^+}_h$ scaled by the average vertical turbulent heat flux ($\overline{w'\theta'}_s$) vs time

Figure 2.15 shows that the velocity component $\overline{w' -}_h$ where $\overline{\theta'}_h > 0$, is effectively scaled by w^* .

The curves representing $\overline{\theta'^+}_h$ where $\overline{w'}_h > 0$ vs time do collapse when scaled by θ^* in Figure 2.16. However it seems this component approaches a constant proportion of $\gamma\Delta h$ in Figure 2.17 indicating that the effects of γ on the positive temperature fluctuations at h may be more important than $(\overline{w'\theta'})_s$.

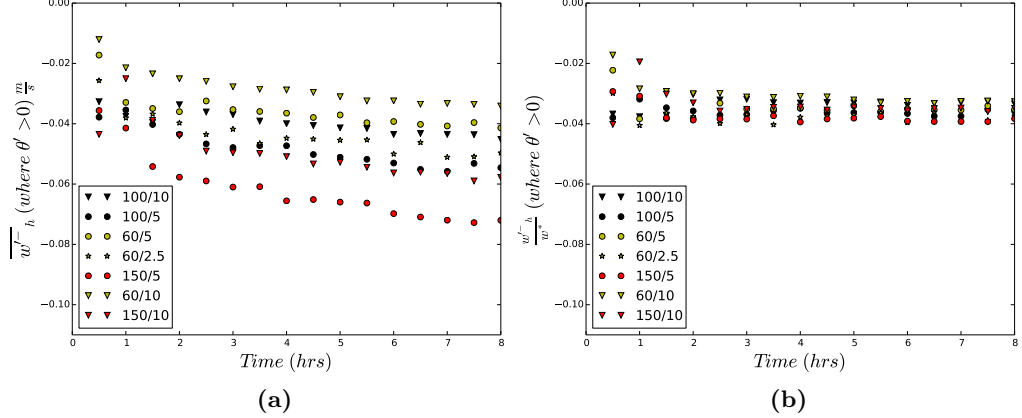


Figure 2.15: (a) Average negative vertical turbulent velocity perturbation at h $\overline{w'^{-} h}$ at points where $\theta' > 0$ and (b) $\overline{w'^{-} h}$ where $\theta' > 0$ scaled by w^* .

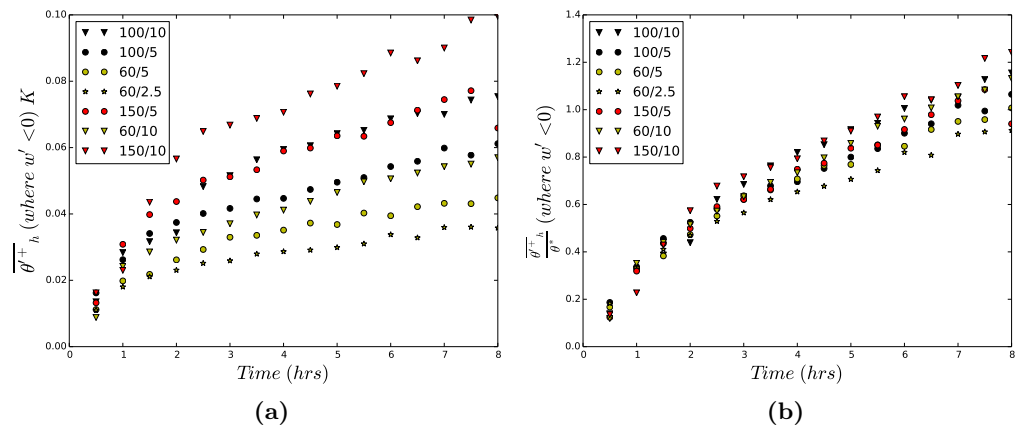


Figure 2.16: (a) Average positive potential temperature perturbation $\overline{\theta'^{+} h}$ at points where $w' < 0$ and (b) $\overline{\theta'^{+} h}$ where $w' < 0$ scaled by θ^* .

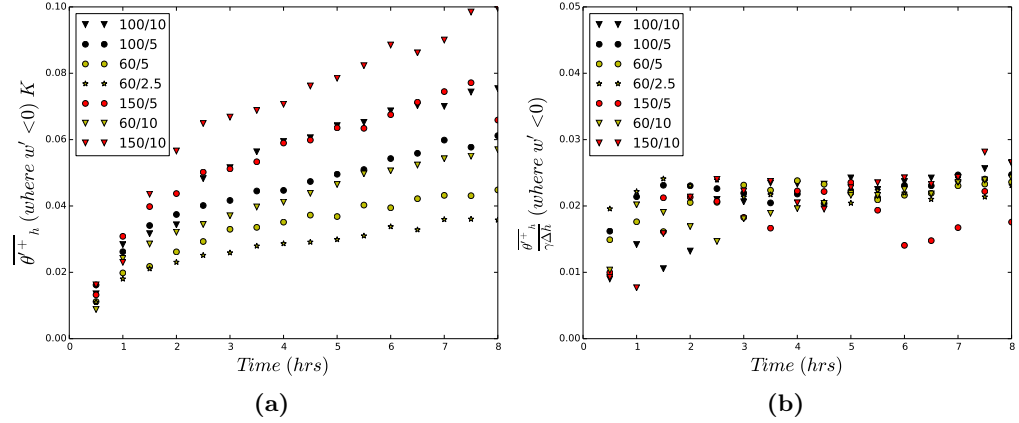


Figure 2.17: (a) Average positive potential temperature perturbation at $h \theta'^+_h$ at points where $w' < 0$ and (b) $\overline{\theta'^+}_h$ where $w' < 0$ scaled by $\gamma \Delta h$.

2.2.4 Answer to Q1

Using a multi-linear regression method, the local ML heights (h_0^l) were determined. Although an ML of uniform value based on the local vertical θ profiles is evident, the region directly above it differs depending on location as well as from the average profile. Since there is no reliable, local definition of h , I take the distributions of local ML height (h_0^l) to be a measure of CBL height variance in space and so the EL. These distributions approached similarity when scaled by h , showing an increase in the lower limit (or percentile) with increased γ . I interpret this result as an indication that increased γ results in a narrower scaled EL depth.

2 dimensional distributions of the local turbulent fluctuations, w' and θ' at h show some variation with γ when scaled by the convective scales w^* and θ^* . The spread of w' narrows while θ' apparently shifts positively.

Plots of the average downward moving quadrant $(\overline{w'} - \overline{\theta'})_h$ at h show dependence on $(\overline{w'} \overline{\theta'})_s$. Breaking $(\overline{w'} - \overline{\theta'})_h$ into its two components reveals dependence on both $(\overline{w'} \overline{\theta'})_s$ and γ . The average downward moving velocity

$(\overline{w'}^-)_h$ at points where there is a positive potential temperature perturbation (θ'^+) show clear dependence on w^* whereas the average positive potential temperature perturbation $\overline{\theta'^+}_h$ where w^- is negative seem to approach a constant value of $\gamma\Delta h$. So the temperature of the entrained warm air depends on γ .

2.3 Relationship of Entrainment Layer Depth to Richardson Number (Q2)

The scaled upper EL limits collapse well in Figure 2.18 (a) to an initial value of approximately 1.15, decreasing to about 1.1. The scaled lower EL limits appear grouped according to γ and increase with respect to time. So overall the scaled EL ($\frac{h_1}{h} - \frac{h_0}{h}$) appears to narrow with time. Whereas, the scaled flux based EL ($\frac{z_{f0}}{z_f} - \frac{z_{f1}}{z_f}$) appears to remain constant with respect to time in Figure 2.18 (b).

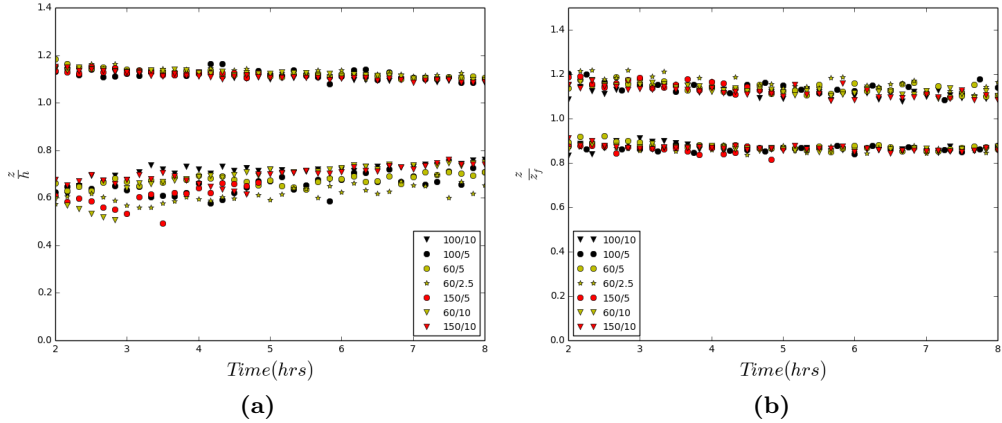


Figure 2.18: (a) Scaled entrainment layer limits ($\frac{h_0}{h}$ and $\frac{h_1}{h}$) vs time and (b) scaled entrainment layer limits ($\frac{z_{f0}}{z_f}$ and $\frac{z_{f1}}{z_f}$) vs time

The lower entrainment layer limit h_0 , as illustrated in Figure 2.19 is the point at which the vertical $\frac{\partial \theta}{\partial z}$ profile exceeds a threshold (.0002), chosen such that it is positive, and at least an order of magnitude smaller than γ . As suggested by Figure 2.11 the resulting scaled EL depth decreases with increasing Richardson number ($Ri = \frac{\frac{g}{\theta_{ML}} \Delta \theta h}{w^{*2}}$ as in Table 2.2). However, grouping of the curves representing

$$\frac{\Delta h}{h} \propto Ri^b \quad (1.15)$$

according to γ is evident in Figure 2.20.

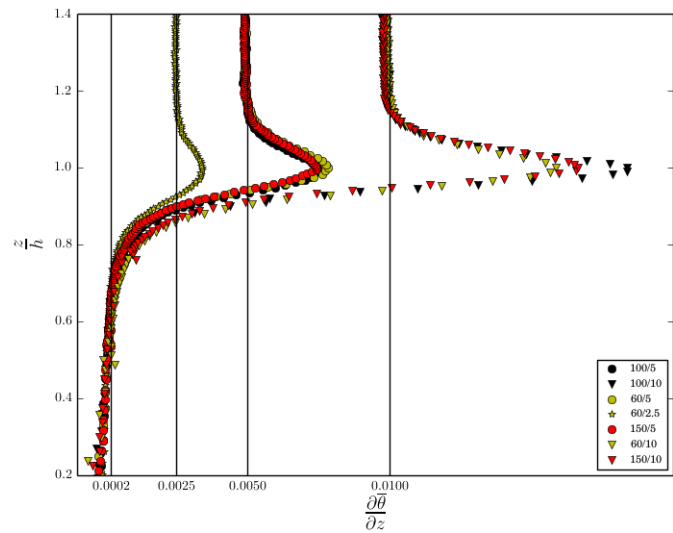


Figure 2.19: Vertical $\frac{\partial \bar{\theta}}{\partial z}$ profiles with threshold at .0002

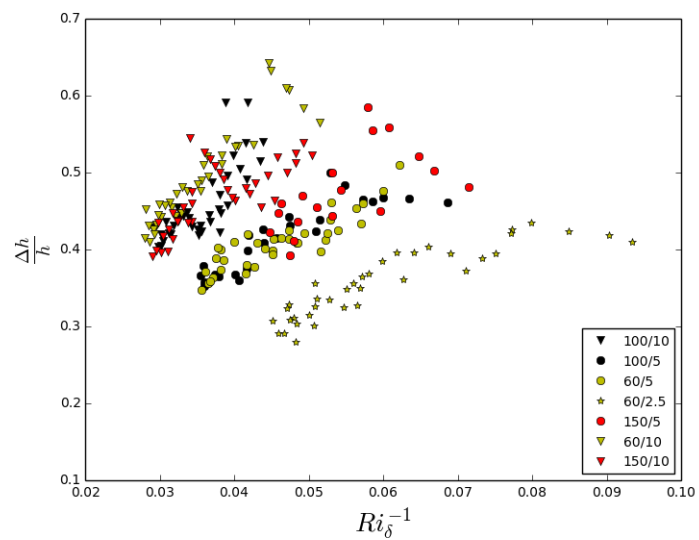


Figure 2.20: Scaled EL depth ($\frac{h_1 - h_0}{h}$) vs inverse Richardson Number with threshold at .0002

2.3.1 Threshold Test for lower EL Limit, h_0

To explore how varying the threshold value effects Equation 1.15, plots analogous to Figure 2.20 were produced at two additional thresholds. In Figure 2.21, a higher value (.0004) results in a higher h_0 and so a narrower EL but a similar grouping according to γ . In Figure 2.22, a lower threshold value (.0001) results in a lower h_0 but also similar grouping according to γ .

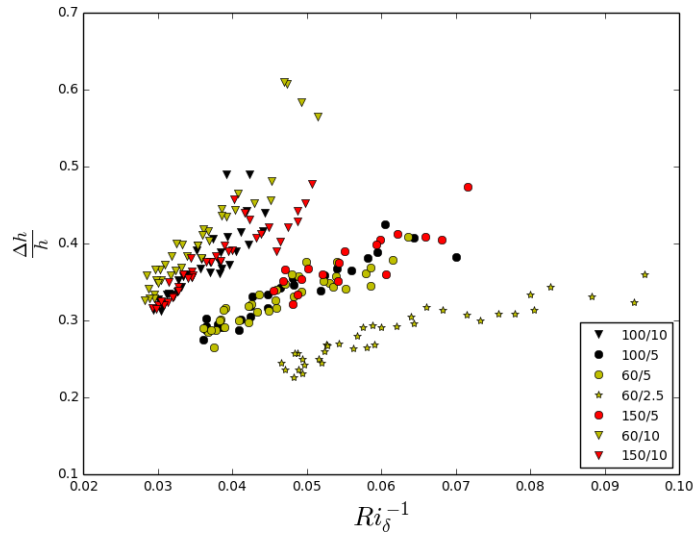


Figure 2.21: Scaled EL depth vs inverse Richardson Number with threshold at .0004

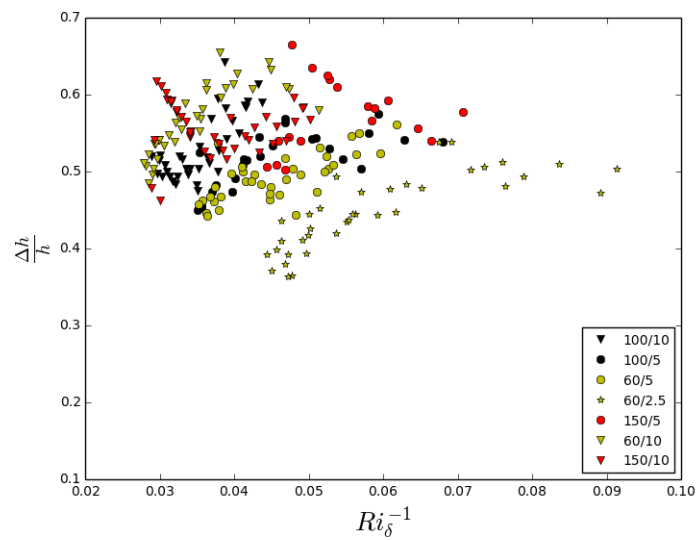


Figure 2.22: Scaled EL depth vs inverse bulk Richardson Number with threshold at .0001

2.3.2 EL Limits based on scaled vertical Profiles

There is a collapsing effect on the scaled Δh vs Ri relationship

$$\frac{\Delta h}{h} \propto Ri^b \quad (1.15)$$

when the heights are defined based on the scaled vertical potential temperature gradient $\frac{\partial \bar{\theta}}{\partial z}/\gamma$ profile in Figure 2.24. This stems from a switch in the relative magnitudes of the vertical potential temperature gradient in the upper ML which can be seen when Figure 2.23 is compared to Figure 2.19. So from here on all heights will be defined based on the scaled average profiles. Figure 2.24 (b) shows little or no Ri dependence when Δh , and so $\Delta\theta$, are based on the $\overline{w'\theta'}$ profile.

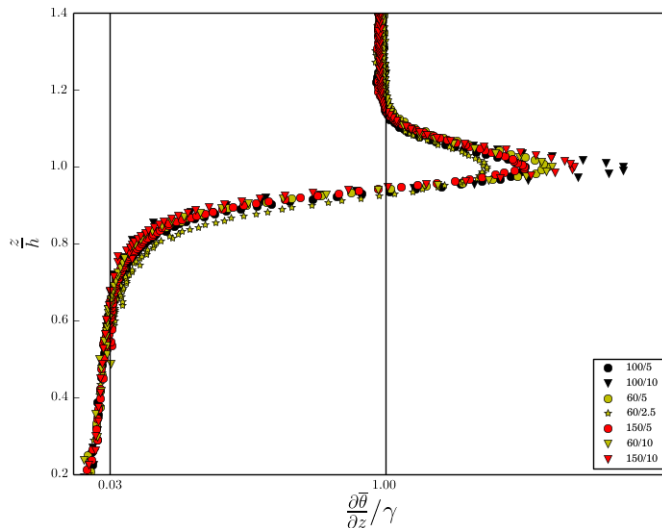


Figure 2.23: Scaled vertical $\frac{\partial \bar{\theta}}{\partial z}$ profiles with threshold at .03

The log-log coordinate plot of Equation 1.15 in Figure 2.25 supports an exponent $b = -\frac{1}{2}$ at lower values of Ri possibly increasing to $b = -1$ at higher Ri .

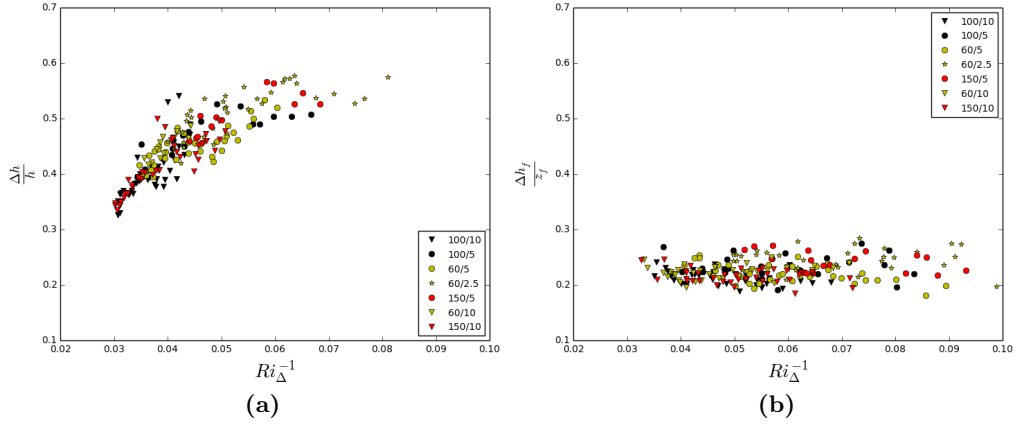


Figure 2.24: Plots of scaled EL depth vs Ri^{-1} . EL limits and so $\Delta\theta$ are based on the vertical $\frac{\partial\theta}{\gamma}$ profile in (a) and the $\frac{\overline{w'\theta'}}{(w'\theta')_s}$ profile in (b).

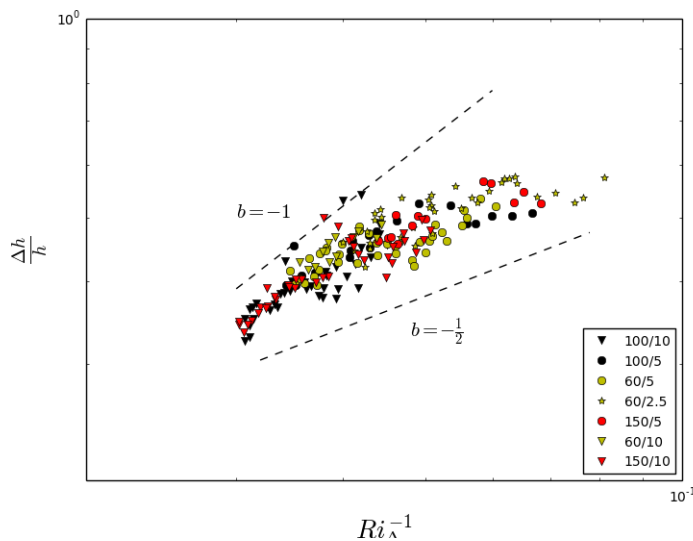


Figure 2.25: Scaled EL depth vs Ri^{-1} based on the $\frac{\partial\bar{\theta}}{\gamma}$ profile in log-log coordinates to see likely values of the exponent b

2.3.3 Answer to Q2

Initially, the CBL height and EL limits are defined based on the vertical $\frac{\partial\bar{\theta}}{\partial z}$ profile. As Brooks and Fowler (2012) point out, when using an average vertical tracer profile there is no universal criterion for a significant gradient. So a threshold value for the lower EL limit (h_0) was chosen such that it was positive, small i.e. an order of magnitude less than γ and the same for all runs. For the sake of rigor, plots of the relationship

$$\frac{\Delta h}{h} \propto Ri^b \quad (1.15)$$

were produced based on two additional threshold values yielding analogous results. In all three cases curves representing Equation 1.15 grouped according to γ

The importance of γ is revealed again as the curves representing equation 1.15 become similar when heights are based on the scaled $\frac{\partial\bar{\theta}}{\partial z}$ profile, $\frac{\partial\bar{\theta}}{\partial z}/\gamma$. Further inspection shows that this change primarily occurs at the lower EL limit (h_0) when $\frac{\partial\bar{\theta}}{\partial z}$ is measured as proportion of γ . The influence of γ on $\frac{\partial\bar{\theta}}{\partial z}$ at h_0 ties in with the influence of γ on downward moving θ'^+ at h shown in Section 2.2.3. This prompts the use of the scaled vertical profiles for the heights (h_0 , h , h_1 and z_{f0} , z_f , z_{f1}) in the subsequent section.

These results support a varying exponent b in Equation 1.15 which is lower in magnitude ($-\frac{1}{2}$) at lower Ri and approaches -1 at higher Ri . For comparison with results from other studies these heights are also based on the vertical $\overline{w'\theta'}$ profiles as shown in Figure 1.5. I find no clear dependence of the scaled EL depth on Ri within this framework.

2.4 Relationship of Entrainment Rate to Richardson Number (Q3)

2.4.1 Reminder of Definitions

A key finding of Section 2.3.2 was that curves representing Equation 1.15 group according to γ when heights are based on the unscaled $\frac{\partial \bar{\theta}}{\partial z}$ and then become similar when heights are based on $\frac{\partial \bar{\theta}}{\gamma}$. So from here on all heights will be as in Figure 2.26 and the corresponding Richardson numbers (R_i) will be as in Table 2.2.

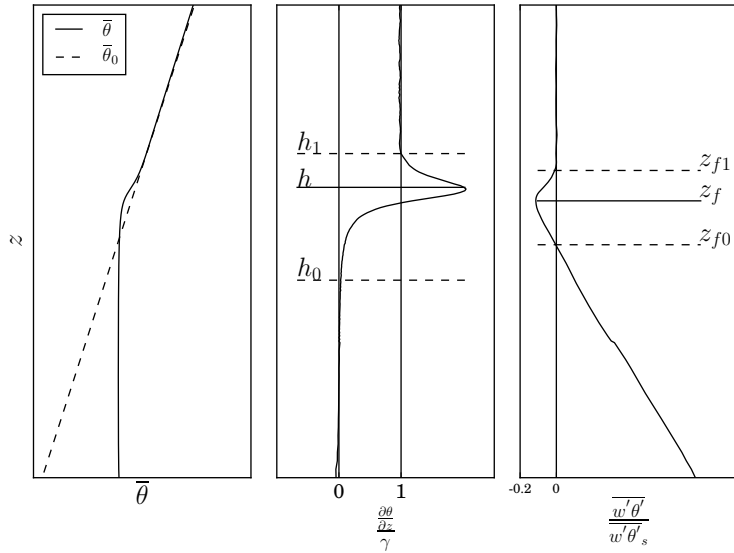


Figure 2.26: Height definitions based on the scaled average vertical profiles. θ_0 is the initial potential temperature.

2.4.2 CBL Growth

Convective boundary layer height (h) in Figure 2.27 grows rapidly initially with a steadily decreasing rate and relates to the square-root of time in Figure 2.28. Federovich et al. (2004) focus on the attainment of a quasi-steady

CBL Height	ML $\bar{\theta}$	θ Jump	Ri
h	$\bar{\theta}_{ML} = \frac{1}{h} \int_0^h \bar{\theta}(z) dz$	$\Delta\theta = \bar{\theta}(h_1) - \bar{\theta}(h_0)$	$Ri_\Delta = \frac{\frac{g}{\bar{\theta}_{ML}} \Delta\theta h}{w^{*2}}$
		$\delta\theta = \bar{\theta}_0(h) - \bar{\theta}_{ML}$	$Ri_\delta = \frac{\frac{g}{\bar{\theta}_{ML}} \delta\theta h}{w^{*2}}$

Table 2.2: Definitions based on the vertical $\bar{\theta}$ profile in Figure 1.5. To obtain those based on the $\overline{w'\theta'}$ profile, replace h_0 , h and h_0 with z_{f0} , z_f and z_{f1}

state regime in which their zero-order model applies. Within this regime scaled CBL height, $hB_s^{-\frac{1}{2}}N^{\frac{3}{2}}$ where B_s is the surface buoyancy flux, relates to the square-root of their scaled time, tN . Over the time of the runs B_s is constant and N varies much more slowly than h . So based on Figure 2.28 I conclude that over the period during which I obtain measurements, all runs are in this quasi-steady state. The height of minimum average heat flux z_f is a constant proportion of h in Figure 2.29 indicating that this point advances more slowly than h .

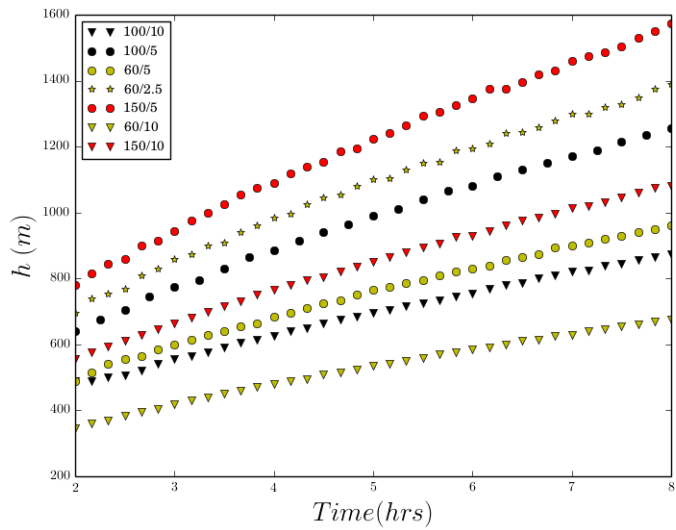


Figure 2.27: h vs time for all runs

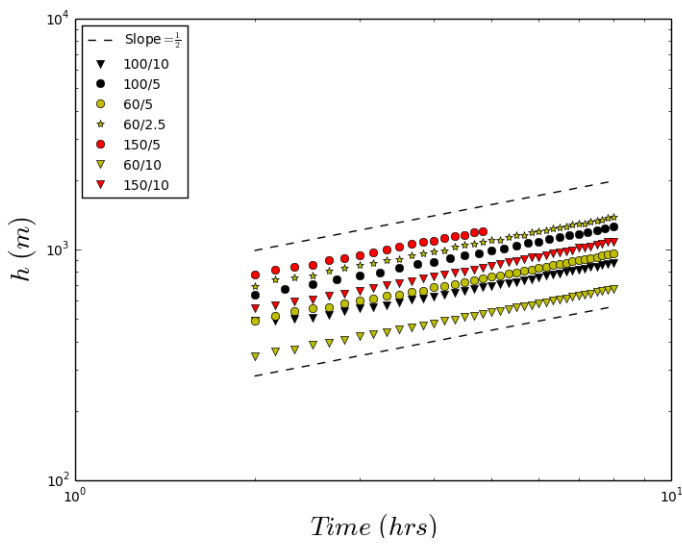


Figure 2.28: h vs time for all runs on log-log coordinates

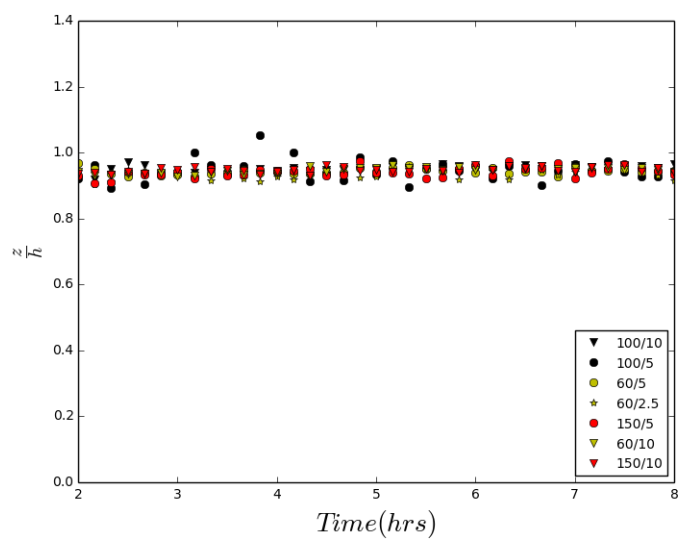


Figure 2.29: $\frac{z_f}{h}$ vs Time

2.4.3 Heights based on the scaled vertical average Potential Temperature Profile

The inverse Richardson numbers (Ri_{Δ}^{-1} and Ri_{δ}^{-1}) in Figure 2.30 decrease in time and group according to γ . There is an overall difference in magnitude since $\Delta\theta > \delta\theta$.

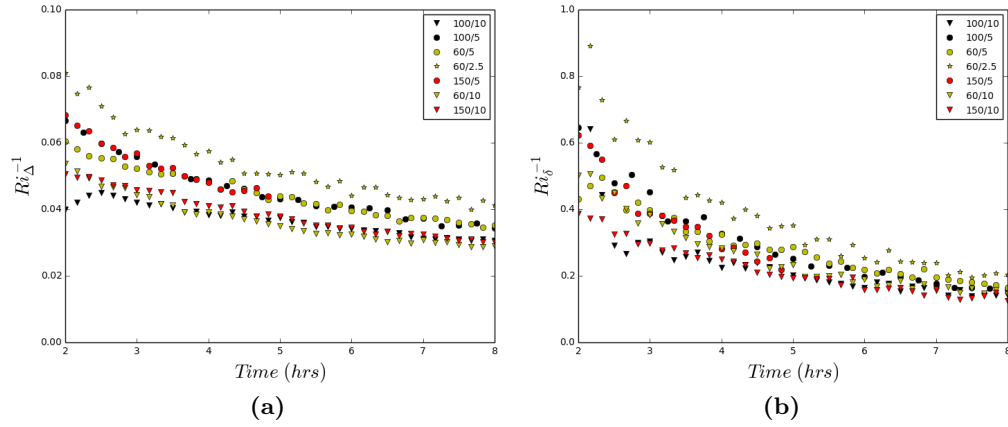


Figure 2.30: Inverse Richardson number vs time based on the $\frac{\partial \bar{\theta}}{\gamma}$ profile using $\Delta\theta$ across the EL in (a) and $\delta\theta$ at h in (b). See Table 2.2.

The entrainment rate ($w_e = \frac{dh}{dt}$) is determined from the slope of a second order polynomial fit to $h(\text{time})$ in Figure 2.27. When w_e is scaled by w^* , the resulting relationship to Ri_Δ plotted in log-log coordinates in Figure 2.31 (a)

$$\frac{w_e}{w^*} \propto \text{Ri}_\Delta^a \quad (2.1)$$

seems to have exponent $a = -1$ at lower Ri_Δ and $a = -\frac{3}{2}$ at higher Ri_Δ .

In Figure 2.31 (b) the relationship

$$\frac{w_e}{w^*} \propto \text{Ri}_\delta^a \quad (2.2)$$

possibly approaches a value of $a = -1$ at higher Ri_δ but a value of lower in magnitude would fit better overall.

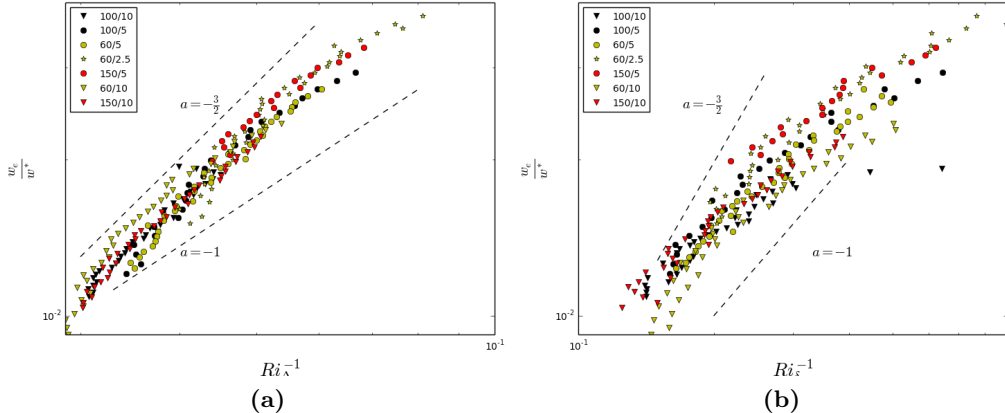


Figure 2.31: Scaled entrainment rate vs inverse Richardson number (Ri^{-1}), in log-log coordinates, where Ri is based on the $\frac{\partial \theta}{\partial z}$ profile using $\Delta\theta$ across the EL in (a) and $\delta\theta$ at h in (b). See Figure 2.26.

2.4.4 Heights based on the scaled vertical average Heat Flux Profile

Richardson numbers with $\Delta\theta$ and $\delta\theta$ based on the $\overline{w'\theta'}$ profile are comparable with those in Section 2.4.3 although Ri_Δ shows considerable scatter in Figure 2.32 (a).

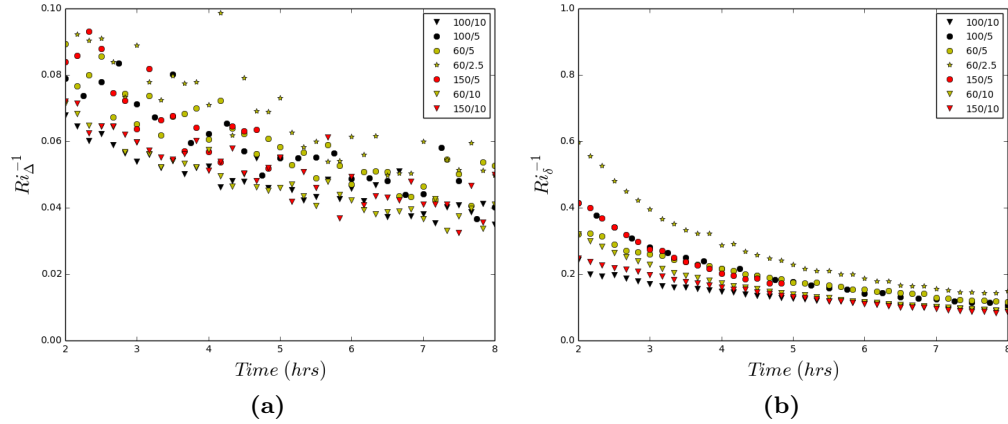


Figure 2.32: Inverse Richardson number vs time based on the $\frac{\overline{w'\theta'}}{\overline{w'\theta'}_s}$ profile using $\Delta\theta$ across the EL in (a) and $\delta\theta$ at z_f in (b). See Figure 1.5.

In Figure 2.33 the axes are in log-log coordinates and all heights are based on the scaled $\overline{w'\theta'}$ profile. The relationship of scaled entrainment rate to Ri_Δ in (a) shows scatter and either value of a or a value in between could fit. Whereas the exponent in the relationship to Ri_δ in (b) seems to change throughout the run(s) and a value less (in magnitude) than -1 might fit better.

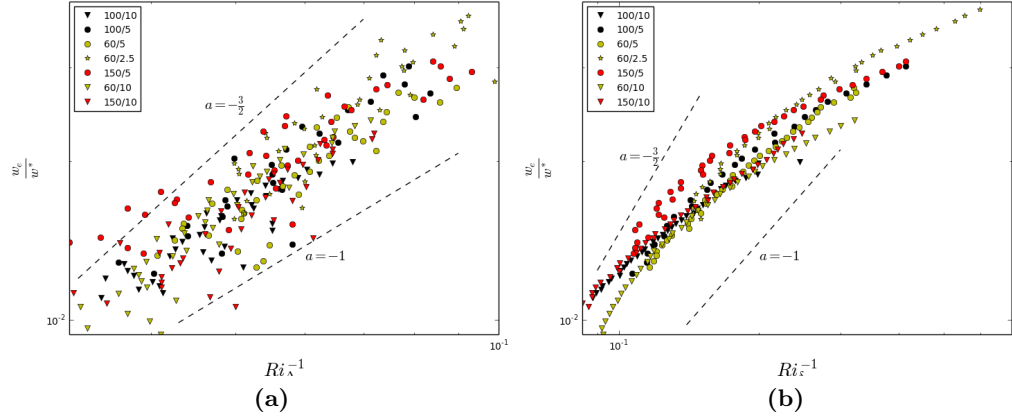


Figure 2.33: Scaled entrainment rate vs inverse Richardson number (Ri^{-1}), in log-log coordinates, where Ri is based on the $\frac{\overline{w'\theta'}}{(w'\theta')_s}$ profile using Δh across the EL in (a) and $\delta\theta$ at z_f in (b). See Figure 1.5.

2.4.5 Answer to Q3

In conclusion the relationship of scaled entrainment rate to Ri_Δ based on the $\frac{\partial \bar{\theta}}{\partial z}$ profile shows the least scatter over time and between runs in Figure 2.31. Here the exponent seems to start at a value close to -1 increasing, with higher Ri , to close to $-\frac{3}{2}$. This apparent change with increased Ri mirrors that seen with Equation 1.15 in Figure 2.25. It's possible that it represents a change in entrainment mechanism as discussed in Section 1.2.6. Overall the definition of the temperature jump certainly has an effect, $\Delta\theta$ yielding a higher value of a than $\delta\theta$.

References

- Batchvarova, E. and S.-E. Gryning, 1994: An applied model for the height of the daytime mixed layer and the entrainment zone. *Boundary-Layer Meteorology*, **71**, 311–323.
- Betts, A. K., 1974: Reply to comment on the paper: "non-precipitating cumulous convection and its parametrization". *Quart. J. Roy. Meteor. Soc.*, **100**, 469 – 471.
- Boers, R., 1989: A parametrization of the depth of the entrainment zone. *Journal of Applied Meteorology*, 107–111.
- Brooks, I. M. and A. M. Fowler, 2012: An evaluation of boundary-layer depth, inversion and entrainment parameters by large-eddy simulation. *Boundary-Layer Meteorology*, **142**, 245–263.
- Crum, T. D., R. B. Stull, and E. W. Eloranta, 1987: Coincident lidar and aircraft observations of entrainment into thermals and mixed layers. *Journal of Climate and Applied Meteorology*, **26**, 774–788.
- Deardorff, J. W., 1970: Convective velocity and temperature scales for the unstable planetary boundary layer and for rayleigh convection. *Journal of the Atmospheric Sciences*, **27**, 1211 – 1213.
- Deardorff, J. W., 1972: Numerical investigation of neutral and unstable planetary boundary layers. *Journal of the Atmospheric Sciences*, **29**, 91 – 115.
- Deardorff, J. W., 1979: Prediction of convective mixed-layer entrainment for realistic capping inversion structure. *Journal of the Atmospheric Sciences*, **36**, 424–436.
- Deardorff, J. W., G. E. Willis, and B. J. Stockton, 1980: Laboratory studies of the entrainment zone of a convectively mixed layer. *J. Fluid Mech.*, **100**, 41–64.

- DuPont, E., J. Pelon, and C. Flamant, 1994: Study of the moist convective boundary layer structure by backscattering lidar. *Boundary Layer Meteorology*, **69**, 1 – 25.
- Federovich, E., R. Conzemus, and D. Mironov, 2004: Convective entrainment into a shear-free, linearly stratified atmosphere: Bulk models reevaluated through large eddy simulation. *Journal of the Atmospheric Sciences*, **61**, 281 – 295.
- Fedorovich, E. and R. Conzemius, 2001: *Large Eddy Simulation of Convective Entrainment in Linearly and Discretely Stratified Fluids*. 1st ed., Kluwer Academic Publishers.
- Garcia, J. R. and J. P. Mellado, 2014: The two-layer structure of the entrainment zone in the convective boundary layer. *Journal of the Atmospheric Sciences*, doi:10.1175/JAS-D-130148.1.
- Kolmogorov, A. N., 1962: A refinement of previous hypotheses concerning the local structure of turbulence in a viscous incompressible fluid at high Reynolds number. *Journal of Fluid Mechanics*, **13**, 82–85.
- Mahrt, L. and J. Paumier, 1984: Heat transport in the atmospheric boundary layer. *Journal of the Atmospheric Sciences*, **41**, 3061–3075.
- Nelson, E., R. Stull, and E. Eloranta, 1989: A prognostic relationship for entrainment zone thickness. *Journal of Applied Meteorology*, **28**, 885–901.
- Schmidt, H. and U. Schumann, 1989: Coherent structure of the convective boundary layer derived from large-eddy simulations. *J. Fluid Mech.*, **200**, 511–562.
- Sorbjan, Z., 1996: Effects caused by varying the strength of the capping inversion based on a large eddy simulation of the shear free convective boundary layer. *Journal of the Atmospheric Sciences*, **53**, 2015 – 2023.
- Sorbjan, Z., 1999: Similarity of scalar fields in the convective boundary layer. *Journal of the Atmospheric Sciences*, **56**, 2212 – 2221.
- Steyn, D. G., M. Baldi, and R. M. Hoff, 1999: The detection of mixed layer depth and entrainment zone thickness from lidar backscatter profiles. *Journal of Atmospheric and Oceanic Technology*, **16**, 953–959.
- Stull, R., 1973: Inversion rise model based on penetrative convection. *Journal of the Atmospheric Sciences*, **30**, 1092–1099.

- Stull, R., 1988: *An Introduction to Boundary Layer Meteorology*. 1st ed., Kluwer Academic Publishers.
- Sullivan, P. P., C.-H. Moeng, B. Stevens, D. H. Lenschow, and S. D. Mayor, 1998: Structure of the entrainment zone capping the convective atmospheric boundary layer. *Journal of the Atmospheric Sciences*, **55**, 3042–3063, doi:10.1007/s10546-011-9668-3.
- Sullivan, P. P. and E. G. Patton, 2011: The effect of mesh resolution on convective boundary layer statistics and structures generated by large eddy simulation. *Journal of the Atmospheric Sciences*, **58**, 2395–2415, doi:10.1175/JAS-D-10-05010.1.
- Tennekes, H., 1973: A model for the dynamics of the inversion above a convective boundary layer. *Journal of the Atmospheric Sciences*, **30**, 558–566.
- Traumner, K., C. Kottmeier, U. Corsmeier, and A. Wieser, 2011: Convective boundary-layer entrainment: Short review and progress using doppler lidar. *Boundary-Layer Meteorology*, **141**, 369–391, doi:10.1007/s10546-011-9657-6.
- Turner, J. S., 1986: Turbulent entrainment: the development of the entrainment assumption and its application to geophysical flows. *J. Fluid Mech.*, **173**, 431–471.
- Vieth, E., 2011: Fitting piecewise linear regression functions to biological responses. *Journal of Applied Physiology*, **67**, 390–396.

A. Appendices

A.1 Potential Temperature: θ

$$\theta = T \left(\frac{p_0}{p} \right)^{\frac{R_d}{c_p}} \quad (\text{A.1})$$

p_0 and P are a reference pressure and pressure respectively.

$$\frac{c_p}{\theta} \frac{d\theta}{dt} = \frac{c_p}{T} \frac{dT}{dt} - \frac{R_d}{p} \frac{dp}{dt} \quad (\text{A.2})$$

If changes in pressure are negligible compared to overall pressure, as in the case of that part atmosphere that extends from the surface to 2Km above it.

$$c_p \frac{d\theta}{\theta} = c_p \frac{dT}{T} - \frac{R_d}{p} \frac{dp}{p} \quad (\text{A.3})$$

$$\frac{d\theta}{\theta} = \frac{dT}{T} \quad (\text{A.4})$$

and if

$$\frac{\theta}{T} \approx 1 \quad (\text{A.5})$$

then small changes in temperature are approximated by small changes in potential temperature

$$d\theta \approx dT \text{ or } \theta' \approx T' \quad (\text{A.6})$$

and at constant pressure change in enthalpy (H) is

$$dH = c_p dT. \quad (\text{A.7})$$

A.2 Second Law of Thermodynamics

$$\frac{ds}{dt} \geq \frac{q}{T} \quad (\text{A.8})$$

For a reversible process

$$\frac{ds}{dt} = \frac{q}{T} \quad (\text{A.9})$$

Using the first law and the equation of state for an ideal gas

$$\frac{q}{T} = \frac{1}{T} \left(\frac{dh}{dt} - \alpha \frac{dp}{dt} \right) = \frac{c_p}{T} \frac{dT}{dt} - \frac{R_d}{p} \frac{dp}{dt} \quad (\text{A.10})$$

so

$$\frac{ds}{dt} = \frac{q}{T} = \frac{c_p}{\theta} \frac{d\theta}{dt} \quad (\text{A.11})$$

For a dry adiabatic atmosphere

$$\frac{ds}{dt} = \frac{c_p}{\theta} \frac{d\theta}{dt} = 0 \quad (\text{A.12})$$

A.3 Reynolds Decomposition and Simplification of Conservation of Enthalpy (or Entropy) for a dry Atmosphere

$$\frac{\partial \theta}{\partial t} + u_i \frac{\partial \theta}{\partial x_i} = \nu_\theta \frac{\partial^2 \theta}{\partial x_i^2} - \frac{1}{c_p} \frac{\partial Q^*}{\partial x_i} \quad (\text{A.13})$$

ν and Q^* are the thermal diffusivity and net radiation respectively. If we ignore these two effects then (adiabatic?)

$$\frac{\partial \theta}{\partial t} + u_i \frac{\partial \theta}{\partial x_i} = 0 \quad (\text{A.14})$$

$$\theta = \bar{\theta} + \theta', \theta = \bar{u}_i + u'_i \quad (\text{A.15})$$

$$\frac{\partial \bar{\theta}}{\partial t} + \frac{\partial \theta'}{\partial t} + \bar{u}_i \frac{\partial \bar{\theta}}{\partial x_i} + u'_i \frac{\partial \bar{\theta}}{\partial x_i} + \bar{u}_i \frac{\partial \theta'}{\partial x_i} + u'_i \frac{\partial \theta'}{\partial x_i} = 0 \quad (\text{A.16})$$

Averaging and getting rid of average variances and their linear products

$$\frac{\partial \bar{\theta}}{\partial t} + \bar{u}_i \frac{\partial \bar{\theta}}{\partial x_i} + u'_i \frac{\partial \theta'}{\partial x_i} = 0 \quad (\text{A.17})$$

Ignoring mean winds

$$\frac{\partial \bar{\theta}}{\partial t} + u'_i \frac{\partial \theta'}{\partial x_i} = 0 \quad (\text{A.18})$$

using flux form

$$\frac{\partial \bar{\theta}}{\partial t} + \frac{\partial (u'_i \theta')}{\partial x_i} - \theta' \frac{\partial u'_i}{\partial x_i} = 0 \quad (\text{A.19})$$

under the bousinesq assumption $\Delta u_i = 0$

$$\frac{\partial \bar{\theta}}{\partial t} = - \frac{\partial (u'_i \theta')}{\partial z} \quad (\text{A.20})$$

ignoring horizontal fluxes

$$\frac{\partial \bar{\theta}}{\partial t} = - \frac{\partial (w' \theta')}{\partial z} \quad (\text{A.21})$$

A.4 Reynolds averaged Turbulence Kinetic Energy Equation

$$\frac{\partial \bar{e}}{\partial t} + \bar{U}_j \frac{\partial \bar{e}}{\partial x_j} = \delta_{i3} \frac{g}{\theta} \left(\bar{u}'_i \theta' \right) - \bar{u}'_i \bar{u}'_j \frac{\partial \bar{U}_i}{\partial x_j} - \frac{\partial \left(\bar{u}'_j e' \right)}{\partial x_j} - \frac{1}{\rho} \frac{\partial \left(\bar{u}'_i p' \right)}{\partial x_i} - \epsilon \quad (\text{A.22})$$

e is turbulence kinetic energy (TKE). p is pressure. ρ is density. ϵ is viscous dissipation.